Tornado Formation and Intensity Prediction Using Polarimetric Radar Estimates of Updraft Area

MICHAEL M. FRENCH[a] AND DARREL M. KINGFIELD[b,c]

[a] *School of Marine and Atmospheric Sciences, Stony Brook University, State University of New York, Stony Brook, New York*
[b] *Cooperative Institute for Research in Environmental Sciences, University of Colorado Boulder, Boulder, Colorado*
[c] *NOAA/Global Systems Laboratory, Boulder, Colorado*

(Manuscript received 28 May 2021, in final form 5 October 2021)

ABSTRACT: A sample of 198 supercells are investigated to determine if a radar proxy for the area of the storm midlevel updraft may be a skillful predictor of imminent tornado formation and/or peak tornado intensity. A novel algorithm, a modified version of the Thunderstorm Risk Estimation from Nowcasting Development via Size Sorting (TRENDSS) algorithm is used to estimate the area of the enhanced differential radar reflectivity factor (Z_{DR}) column in Weather Surveillance Radar–1988 Doppler data; the Z_{DR} column area is used as a proxy for the area of the midlevel updraft. The areas of Z_{DR} columns are compared for 154 tornadic supercells and 44 nontornadic supercells, including 30+ supercells with tornadoes rated EF1, EF2, and EF3; 8 supercells with EF4+ tornadoes also are analyzed. It is found that (i) at the time of their peak 0–1-km azimuthal shear, nontornadic supercells have consistently small ($<20\,km^2$) Z_{DR} column areas, while tornadic cases exhibit much greater variability in areas; and (ii) at the time of tornadogenesis, EF3+ tornadic cases have larger Z_{DR} column areas than tornadic cases rated EF1/2. In addition, all eight violent tornadoes sampled have Z_{DR} column areas $> 30\,km^2$ at the time of tornadogenesis. However, only weak positive correlation is found between Z_{DR} column area and both radar-estimated peak tornado intensity and maximum tornado path width. Planned future work that focuses on mechanisms linking updraft size and tornado formation and intensity is summarized and the use of the modified TRENDSS algorithm, which is immune to Z_{DR} bias and thus ideal for real-time operational use, is emphasized.

KEYWORDS: Tornadogenesis; Severe storms; Supercells; Tornadoes; Radars/Radar observations; Nowcasting

1. Introduction

Operational forecasters face a number of challenges in attempts to skillfully ''nowcast'' (i.e., 0–1-h forecasts) the tornado life cycle. Here, we break up the life cycle simply into tornadogenesis, tornado intensification, and tornado dissipation. Difficulty in understanding and prediction in any of these stages derives from the small spatiotemporal scales over which relevant processes are thought to occur, which makes them difficult to observe. Most research efforts have focused on determining the likelihood for supercell tornado formation, given the severe impacts strong and violent tornadoes, which largely occur in supercells (Smith et al. 2012), can have on people and property. Unfortunately, knowledge of the supercell tornadogenesis process is incomplete (e.g., Markowski and Richardson 2009), and while tornado-supportive environments may be identified (e.g., Rasmussen and Blanchard 1998; Thompson et al. 2003; Markowski et al. 2003; Parker 2014; Coffer et al. 2019), they are general and inexact. In addition, tornadic and nontornadic supercells contain largely the same appearance via traditional radar variables (e.g., Trapp 1999; Klees et al. 2016), which is troublesome when weather radar is the most readily available real-time convective storm observational tool. There is some preliminary support for differentiating between tornadic and nontornadic supercells using polarimetric radar data (e.g., Kumjian and Ryzhkov 2008a; French et al. 2015; Van Den Broeke 2020; Homeyer et al. 2020), particularly recently in Loeffler et al. (2020), who found statistically significant differences in a polarimetric signature in a large sample of supercell cases.

There has been comparatively less focus in the literature on nowcasting tornado intensification and dissipation. Regarding the latter, the reader is referred to Marquis et al. (2012) for a summary of dissipation mechanisms and French and Kingfield (2019) and Segall et al. (2021) for how those mechanisms may be translated to radar ''fingerprints'' for use in nowcasting tornado dissipation.

Regarding the former, there is some skill in using environmental approaches to better predict conditions favorable for more intense tornadoes (e.g., Thompson et al. 2012; Coffer et al. 2019), especially in combination with radar data (Smith et al. 2020b). But there are not simple radar *signatures or behaviors* known to skillfully predict peak tornado intensity. Complicating matters, data from rapid-scan radars provide evidence that tornado intensity can vary over short time scales and in height (e.g., French et al. 2014; Griffin et al. 2019; McKeown et al. 2020), and processes supporting tornado intensification and their relationship to genesis processes are poorly understood (e.g., Marquis et al. 2016). Recent work also has provided evidence that the intrinsic modeling predictability of supercell tornado intensity is low, even in environments that are strongly supportive of tornadoes (Markowski 2020). Therefore, after a tornado forms, forecasters are largely left to monitor near-real-time, near-surface tornado intensity estimates and have few tools with which to predict peak tornado intensity as a tornado forms. Yet it is important for forecasters to monitor tornado evolution to optimize information to the public and emergency management. Peak intensity information in particular may be

Corresponding author: Michael M. French, michael.m.french@stonybrook.edu

DOI: 10.1175/WAF-D-21-0087.1

used in impact-based warnings, which have been shown to be an effective communication tool in hazardous weather situations (Ripberger et al. 2015; Casteel 2016).

Current tools available to assess tornado intensity using WSR-88D data are mostly diagnostic. Radial velocity within a tornadic vortex signature (TVS) can be used to estimate current intensity (e.g., Burgess et al. 2002) but assumes a number of approximations (Wood and Brown 1997; Snyder and Bluestein 2014). Radar data can be combined with other observational data to develop probability-based intensity assessments (e.g., Smith et al. 2015, 2020a; Thompson et al. 2017). Estimates of tornado intensity also can be developed using radar data in algorithms (e.g., Kingfield and LaDue 2015). The height of the polarimetric tornadic debris signature (TDS; Ryzhkov et al. 2005) has been used in concert with velocity data to estimate tornado intensity (Gibbs 2016). Other approaches combined previous work into a statistical model to assess near-real-time tornado intensity (Cohen et al. 2018). However, most of these approaches require information about a tornado, typically some measure of low-level rotation, that already has formed. In addition, because estimates of rotational velocity will suffer at greater ranges from the radar, so will efforts to use rotational velocity to assess tornado intensity potential (e.g., Smith et al. 2015). Recently, Gibbs and Bowers (2019) did display some skill in *anticipating* significant tornado damage using WSR-88D rotational velocity combined with mesocyclone depth information, though skill scores were still highest using data from right before the onset of significant damage.

One possibility for tornado intensity prediction derives from work in Trapp et al. (2017; hereafter T17). They argued using theory and model simulations, that wider storm updrafts should lead to both wider and stronger tornadoes based on conservation of angular momentum arguments. In modeling simulations, T17 found support for their hypothesized relationships via strong linear correlations among updraft area, downdraft area, mid-level mesocyclone area, near-ground mesocyclone area, and, importantly, near ground vertical vorticity (e.g., Fig. 1a). In addition, updraft area was strongly influenced by vertical wind shear, which is consistent with past (Kirkpatrick et al. 2009) and more recent work (e.g., Warren et al. 2017; Marion and Trapp 2021; Peters et al. 2019).

Seeking out observational support for the T17 hypothesis is complicated by the difficulty in observing supercell updrafts and/or mesocyclones in conventional remote sensing data. T17 found in their simulations that there should be a strong relationship between the area of a satellite-observed overshooting top (OT) and midlevel updraft area, and concluded that OTs may be used to predict tornado intensity. In a follow-up study of 30 tornadic storms, Marion et al. (2019) found large differences between the OT area of storms with tornadoes rated EF3+ and those rated EF0–2 (Fig. 1b), though only nine EF3+ tornadic storms were sampled. Likewise, they found relationships between OT area and tornado wind speeds associated with the surveyed EF scales, even after accounting for uncertainties in the wind speed estimates.

Most relevant to this study is Sessa and Trapp (2020), who used WSR-88D data in 102 tornado-producing convective storms to relate the approximate low-level mesocyclone width prior to tornadogenesis (via radial velocity data) to peak tornado intensity. They found a robust and significant relationship, particularly in supercells, between averaged (in both height and time) mesocyclone width and tornado intensity estimated both via EF scale (Fig. 1c) and maximum sum of the inbound and outbound radial velocities (ΔV) in the tornadic

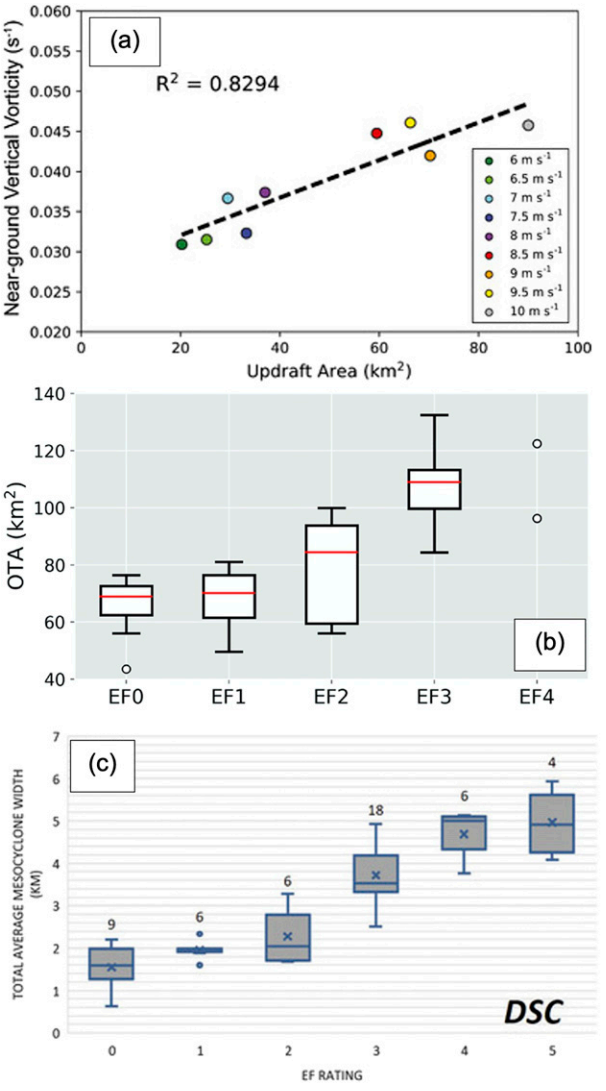

FIG. 1. (a) Scatterplot showing relationship between supercell midlevel (z = 6.25 km) updraft area (km^2) and near-ground vertical vorticity (s^{-1}) from CM1 experiments over a range of hodograph radii (m s^{-1}). Adapted from Trapp et al. (2017). (b) Box-and-whisker plot of observed overshooting top area (OTA; km^2) vs tornado EF scale rating for 30 tornadic supercells. Adapted from Marion et al. (2019). (c) Box-and-whisker plot showing the relationship between the total average pre-tornadic mesocyclone width (km) and EF rating of the resultant tornado for 49 discrete supercells. The mean is represented by the × and the median by the bar. The top and bottom of the box represent the third and first quartiles with exclusive medians, respectively, and the top and bottom whiskers represent the minimum and maximum values, respectively. Adapted from Sessa and Trapp (2020).

vortex signature (TVS). The authors also found strong linear relationships between mesocyclone width and estimated tornado width and pathlength. The combination of prior theoretical and modeling support with these observational studies provides motivation to further refine relationships between supercell updraft area proxies and peak tornado intensity, ideally in a large number of cases.

However, other studies offer criticism of and/or evidence countering the T17 hypothesis. Coffer and Markowski (2018) performed 30 simulations using composite environmental profiles in supercells observed in the second Verification of the Origins of Rotation in Tornadoes Experiment (VORTEX2; Wurman et al. 2012) and found highly variable updraft widths and much weaker correlations among the same parameters studied in T17 despite only subtle changes to the environmental profile. In response, Trapp et al. (2018) updated their simulations using finer grid spacing (similar to that used in Coffer and Markowski 2018) and again found strong linear correlations between updraft size and near-surface vertical vorticity. They argued that their greater range of bulk shear profiles better reflected the true range seen in tornadic environments compared to those in Coffer and Markowski (2018). Other recent studies have not found strong relationships between updraft width and near-surface vortex intensity in simulated supercells (Fischer and Dahl 2020; Goldacker and Parker 2021).

We are not aware of any work that has focused on moving beyond traditional radar variables and products derived therein to examine the use of polarimetric radar data to *predict* peak tornado intensity. Despite disagreement in the literature, we believe that the results from T17, Marion et al. (2019), and Sessa and Trapp (2020) introduce one possibility to do so: using columns of enhanced differential radar reflectivity factor (Z_{DR}) as an updraft proxy. Elevated Z_{DR} above the 0°C level adjacent to or collocated with updrafts have been observed repeatedly in convective storms (e.g., Illingworth et al. 1987; Conway and Zrnić 1993; Ryzhkov et al. 1994; Brandes et al. 1995), including in supercells (e.g., Loney et al. 2002; Kumjian and Ryzhkov 2008b; Kumjian et al. 2010; Snyder et al. 2013). The signature results from the lofting of large rain drops ($Z_{DR} > 0$ dB) by the storm updraft above the 0°C level where there is otherwise typically dry snow aggregates with Z_{DR} near 0 dB (e.g., Kumjian et al. 2014). An updraft that is wider and larger should then also have a greater area over which the lofting process occurs leading to a larger Z_{DR} column, assuming that its vertical velocities are large enough to loft hydrometeors over the extended area.

Indeed, Z_{DR} column area was one of several "metrics" tested by Van Den Broeke (2017) to examine if there were differences among tornadoes of different intensities, among other tornado subgroups. In that study, Z_{DR} column areas in significantly tornadic storms were larger than in weakly tornadic storms. However, only seven EF3+ tornadoes were analyzed and Z_{DR} column areas were averaged over variable time increments (30–90+ min). Most importantly, the study did not examine whether Z_{DR} column area was *predictive* of tornado intensity differences.

Previous studies also have found correlations between updraft strength and heights of Z_{DR} columns (Kumjian et al. 2014), and Picca et al. (2010) found correlations between Z_{DR} column height and width and lagged low-level Z_H. Potential operational utility of the signature led to the development of an automated Z_{DR} column algorithm for WSR-88D use (Snyder et al. 2015). More recent work has found that Z_{DR} columns may be used operationally to distinguish between severe and nonsevere storms, particularly for wind and hail (Kuster et al. 2019). Also, while there is no explicit evidence that Z_{DR} column heights may be used to distinguish between tornadic and nontornadic supercells (Picca et al. 2015; Kuster et al. 2019; Van Den Broeke 2020), Van Den Broeke (2020) found differences in the areas of Z_{DR} columns between "pre-tornadic" and nontornadic supercells, though the study again utilized averaging areas for each case over several, and different numbers of volumes.

Neither Z_{DR} column width nor area has specifically been evaluated for potential operational *predictive* utility for tornado *intensity*. The dual-polarization upgrade of the WSR-88D completed in 2013 provides the potential to analyze the Z_{DR} columns associated with a large number of tornadic storms to determine if a proxy for updraft width may be able to skillfully predict tornado intensity. Also, preliminary evidence in Van Den Broeke (2020) combined with the known relationship between vertical wind shear and updraft size motivates us to also explore if Z_{DR} columns may be larger in tornadic supercells compared to nontornadic supercells. Indeed, though it was not the focus of their study, Coffer and Markowski (2018) found generally larger midlevel mesocyclone and updraft areas in their tornadic supercell simulations compared to their nontornadic supercell simulations (see their Fig. 4). This paper serves as one in an ongoing series of climatological studies of WSR-88D polarimetric characteristics of supercells (French and Kingfield 2019; Loeffler et al. 2020; Tuftedal et al. 2021; Segall et al. 2021). Section 2 discusses data and methods. Section 3 presents comparisons of Z_{DR} column areas in supercells with tornadoes of varying intensities and for tornadic versus nontornadic supercells. Results and their implications are summarized and discussed in section 4.

2. Data and methods

a. Case selection

A priority of this study was to analyze a sufficient number of supercell cases per interval (i.e., ideally 30+ tornadic cases for *each* EF scale bin and 30+ nontornadic supercells) in order to establish or refute a true signal in the relationships between Z_{DR} column area, the tornadogenesis process, and tornado intensity. First, in order to accrue a sufficient number of cases for the tornado intensity part of the study, a storm mode database compiled by the Storm Prediction Center (SPC) for years 2013–17 (Smith et al. 2012) was interrogated for tornadoes that formed between 20 and 60 km in range from a WSR-88D site so that intensity estimates via ΔV calculations were confined to the lowest ~500-m layer. The initial group of cases was then manually analyzed to eliminate cases in which the cyclic tornadogenesis/mesocyclogenesis process was observed and the tornado in question was not the first tornado in a "family," so that complications from the presence of multiple

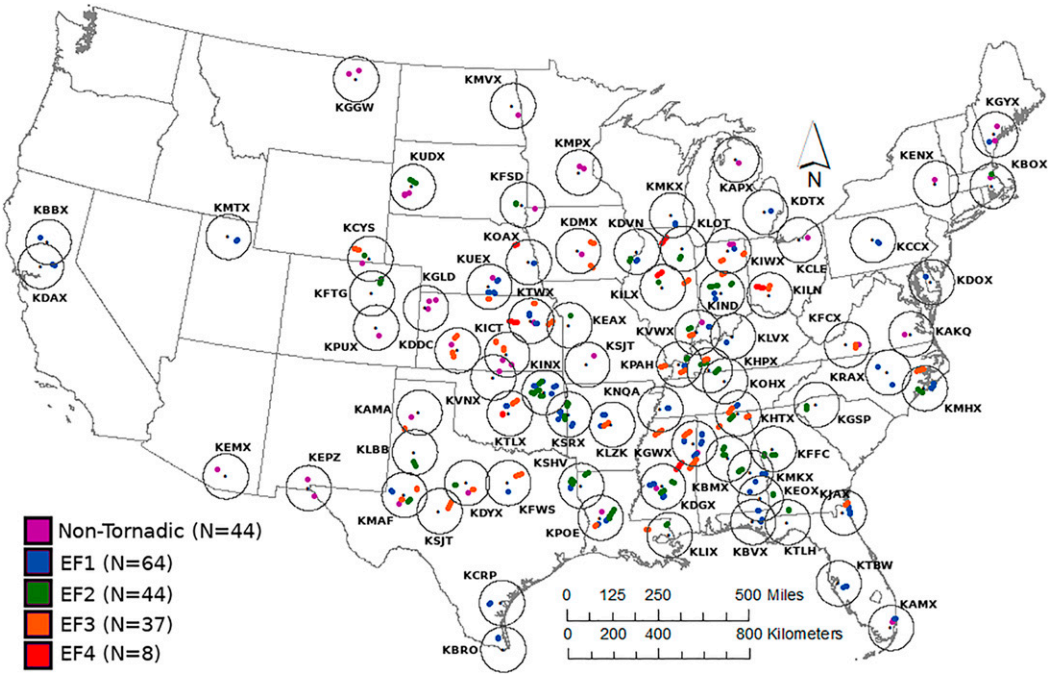

FIG. 2. Map of all tornadic and nontornadic supercell cases used in this study. The tornadic cases are color coded by surveyed EF scale intensity and the location marks the approximate tornadogenesis location from *Storm Data*. For the nontornadic cases, the location is that of the peak 0–1-km azimuthal shear at the analysis time used in this study (i.e., the tornadogenesis failure time). The location of the WSR-88D used for each case and its 100-km range ring also are shown.

updrafts (e.g., Dowell and Bluestein 2002) could be mitigated. The remaining cases were then separated out by EF scale and refined.

In this study, we examined Z_{DR} column areas separately for tornadoes rated EF1, EF2, EF3, and EF4+. EF0 tornadoes were not analyzed, owing to the likelihood of large underrate biases in strong tornadoes over open country (e.g., Alexander 2010; Bluestein et al. 2018; Wurman et al. 2021). Our methodology provided sufficient samples of EF1 and EF2 cases that contained an identifiable Z_{DR} column. However, the aforementioned criteria left only 17 (3) EF3 (EF4+) cases, so 2018–20 data also were interrogated, and the 60-km range restriction was relaxed to 100 km for EF3+ cases. The additional three years of data and longer range criterion yielded an additional 15 (5) cases for a total of 33 (8) cases. The EF1–2 cases were analyzed chronologically until a similar number of cases were reached; analysis from 2013 to 2016 brought in 36 EF1 supercells and analysis from 2013 to 2017 led to 32 EF2 supercells. Therefore, a total of 109 tornadic supercell cases with Z_{DR} columns were analyzed. Subsequent analysis also included 45 cases in which no Z_{DR} column was identified at the analysis times. Cases were not "pre-screened" for the presence of a Z_{DR} column, and "no-column" cases were included only from the set that already had been analyzed (e.g., only no-column cases from 2013 to 2016 were included for EF1 cases).

The initial pool of nontornadic cases is the same one as that detailed in Loeffler et al. (2020) and Tuftedal et al. (2021). Cases were chosen using a 2015 SPC database that associated each severe report (severe criteria hail and wind, tornado) with a storm mode. Supercells that were not associated with a tornado and within 20–60 km of a WSR-88D were included for possible analysis. All nontornadic cases were then manually verified to have a midlevel mesocyclone and lack a TDS. The restrictions led to a total of 44 nontornadic storms used in this study, including cases both with and without Z_{DR} columns.

The location of cases in the United States (Fig. 2) shows a weighting toward cases in the southern plains and Deep South. This is especially true in this study as we required our set of cases to have nearly equal numbers of EF1–3 cases, and the more intense tornadoes in particular tend to occur in these locations. Therefore, the sample of cases analyzed herein does not represent the surveyed tornado intensity distribution in the United States as a whole. Most cases analyzed (91%) were separated from other cases by at least one hour in time and/or were far enough away from each other that they were scanned by different WSR-88D systems, thus our analysis is not biased by clusters of storms that formed in close proximity to each other.

b. *Calculation of Z_{DR} column area*

To identify regions where a Z_{DR} column is located, this study employs a modified approach to that used in Segall et al. (2021). In their study, Z_{DR} column regions were defined using the copolar cross correlation coefficient at lag zero (ρ_{HV}) >0.8 and Z_{DR} >1.0 dB in the scan nearest to 1 km above the 0°C level as defined by the 13-km Rapid Refresh (RAP; Benjamin

et al. 2016) analysis grid. They corrected for potential Z_{DR} biases through the use of external target methods calculated at the WSR-88D Radar Operations Center (Richardson et al. 2017). These methods compare observed Z_{DR} values to light rain, dry snow, and Bragg scatter conditions with intrinsic Z_{DR} values to estimate the bias. While these techniques can help offset a biased Z_{DR}, they are imperfect, particularly in the case of the light rain technique (Richardson and Lee 2019). An alternative originates from Kingfield and Picca (2018), who introduced a Thunderstorm Risk Estimation and Nowcasting Development from Size Sorting (TRENDSS) algorithm. TRENDSS calculates the standard score of unique Z_H–Z_{DR} relationships for each radar elevation scan to identify positive Z_{DR} outliers. This highlights regions where hydrometeor size sorting is occurring and can indicate the location of an updraft. Given that a Z_{DR} bias is typically uniform across the radar scanning range, the calculation of standardized Z_{DR} anomalies would incorporate this bias and render the output immune to miscalibration.

This study extends the methodological work of Segall et al. (2021) by taking a TRENDSS analog approach to identifying Z_{DR} column regions. For each elevation angle of radar data, a sample of Z_{DR} bins was collected that met the following three criteria: 1) $\rho_{HV} > 0.8$ to remove potential nonmeteorological scatterers, 2) $Z_{DR} < 6$ dB to remove possible biological scatterers, and 3) the radar bin was in a region between 1 km below and 5 km above the 0°C level as defined from the 13-km RAP. For each Z_{DR} bin collected in the set, the standard score was calculated using the mean and standard deviation (SD) of Z_{DR} from the entire sample set, which only included data that met the aforementioned criteria. The result is a field of Z_{DR} anomalies with each bin corresponding to the number of SDs from the mean for each elevation angle.

Region growing allows for neighboring elements in an image exceeding some value to be joined together into a new group (Lakshmanan 2012). We apply this technique to combine spatially connecting regions exceeding either 1 or 2 SDs into a new radar image and assign each cohesive group of bins with a unique identifier. Once each region is defined, the area of each region is calculated as the sum of the areas of each radar bin that comprises that region and it is plotted in the same polar coordinate space as the other radar moments for that elevation angle and time. Similar to Segall et al. (2021), we defined the Z_{DR} column of interest as the location nearest to the main updraft of the thunderstorm being examined on the radar scan closest to 1 km above the 0°C level. The latter criterion ensured this version of TRENDSS is focused on updraft identification instead of raindrop size sorting in an environment with nonzero storm-relative flow.

To compare the modified TRENDSS approach to a more standard Z_{DR} column identification method, we also determined Z_{DR} column regions using the Segall et al. (2021) approach for a subset of 44 tornadic cases (Fig. 3). There are very high linear correlations between the Segall et al. (2021) methodology and both the one and two SD modified TRENDSS approach. For larger columns, the SD1 (SD2) tends to have larger (smaller) column areas than the traditional method. Given the high correlations between methods and the TRENDSS approach

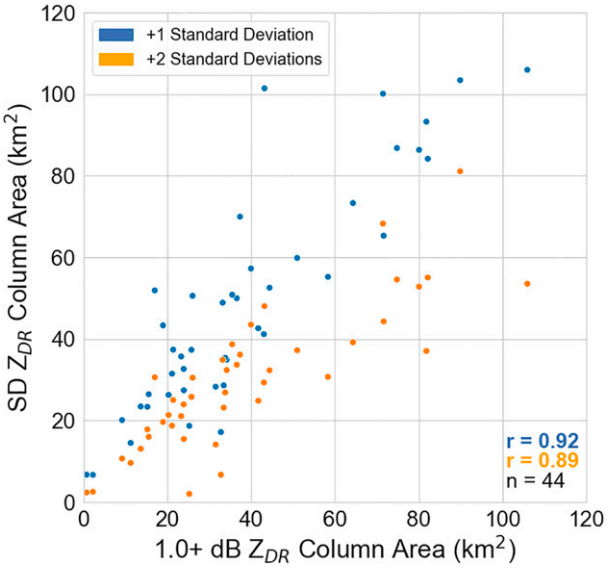

FIG. 3. Comparison between Z_{DR} column area calculations using Z_{DR} values of 1 dB and larger and that using the modified TRENDSS algorithm. Two versions of the TRENDSS algorithm are employed, one defines a Z_{DR} column as having Z_{DR} values that are at least one standard deviation above the baseline (blue) and the second defines a Z_{DR} column as having Z_{DR} values that are at least two standard deviations above the baseline (orange). The Pearson correlation coefficients and the sample size for each of the two comparisons are shown in the bottom right.

immunity to Z_{DR} biases, the results presented herein will use the TRENDSS methodology. And because we sometimes had to throw out cases because of melting layer interference from large columns (see section 2c), we chose to use the SD2 approach.

Some previous studies have analyzed updraft width proxies instead of updraft area proxies. We developed an algorithm for determining Z_{DR} column area rather than width because of the tendency for Z_{DR} columns to be amorphous, which makes width determination difficult. Though updraft area and width are related, this study is not directly measuring proxies for updraft width. Similarly, the calculations of area often included 2–3 adjacent areas in the column region. In this study, the column area is the summed total of the individual areas,[1] which we believe better captures the updraft size compared to taking the maximum contiguous area value. In addition, one may wonder if updraft area varies with height. The use of Z_{DR} columns limited us to observations above the 0°C level to

[1] Summing individual areas together has to be done manually and is the subjective part of using this version of TRENDSS. Outside of melting layer interference, in most cases, it was not difficult to identify that multiple large areas were clearly part of the Z_{DR} column. And in cases when it was not obvious if a smaller area was part of the Z_{DR} column (see section 2c), it is unlikely that the decision noticeably affected the overall area of the Z_{DR} column used in our analyses.

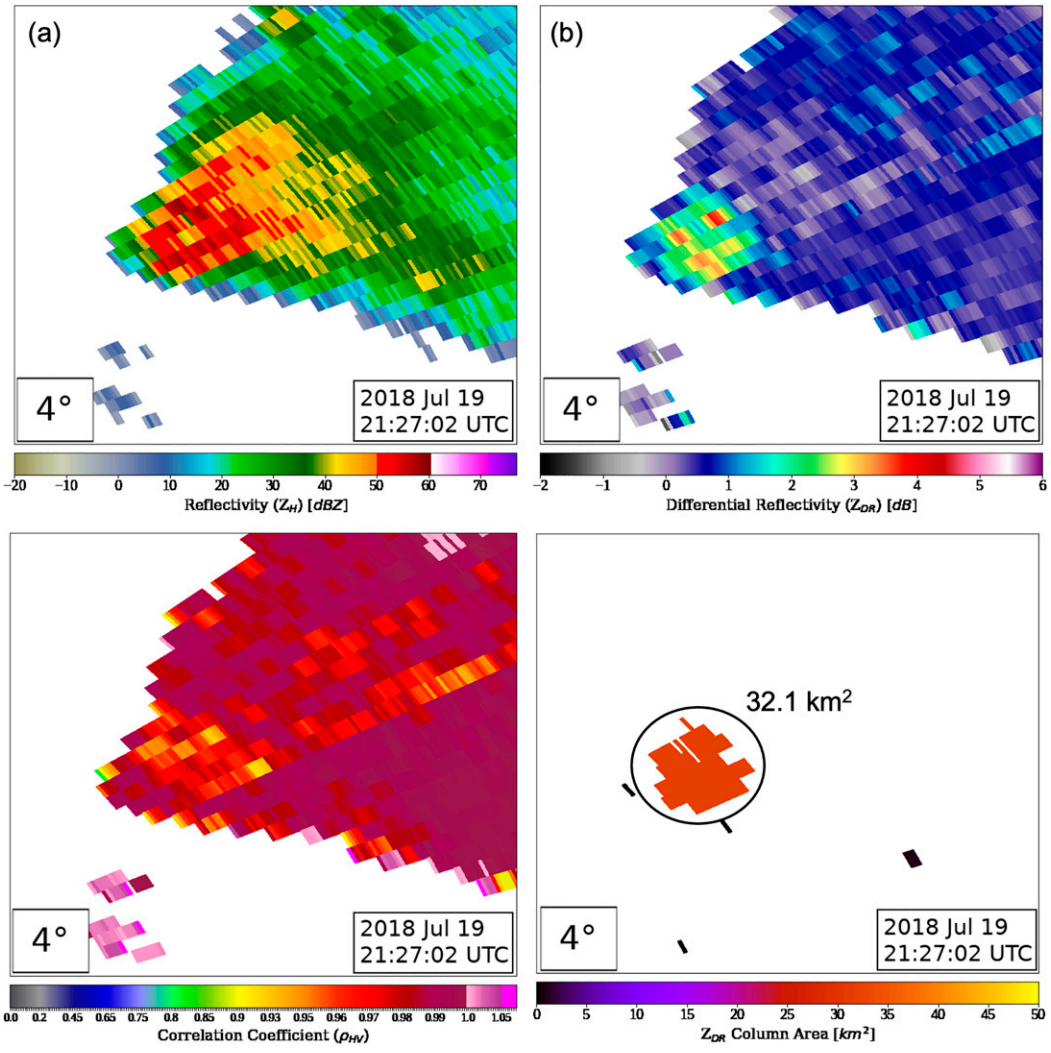

FIG. 4. Example of the modified TRENDSS algorithm identification of a Z_{DR} column using the two standard deviation approach discussed in the text for an EF3 tornadic case on 19 Jul 2018. (a) Radar reflectivity factor (dBZ), (b) Z_{DR} (dB), (c) copolar correlation coefficient, and (d) Z_{DR} column area (km^2) from the modified TRENDSS algorithm. The area representative of the Z_{DR} column is enclosed by a circle; the area value is also shown in (d).

approximate the size of the updraft, and the higher in the storm above the 0°C level we used, the fewer cases there were in which a Z_{DR} column could be identified. Also, results from supercell simulations have shown little change in the actual supercell updraft area with height above 3 km (e.g., Peters et al. 2019). An example of the algorithm output for a tornadic case from 19 July 2018 (Figs. 4a–c) is shown (Fig. 4d).

c. *Data quality control*

The calculation of Z_{DR} column area in this study required data from two polarimetric variables: Z_{DR} and ρ_{HV}. The former variable is susceptible to potentially large errors owing to the effects of differential attenuation and biases. Differential attenuation is of limited concern in this study, owing both to the use only of S-band radar data, which has low attenuation coefficients, and the focus of data analysis above the melting layer where there are smaller areas of large Z_H and Z_V. As discussed in section 2b, the development of the modified TRENDSS product explicitly renders Z_{DR} bias moot, eliminating the serious concerns about real-time use of Z_{DR} data in analyzing quantifiable fields. The use of S-band data in this study also mitigates concerns about the use of Z_{DR} as a drop size proxy given the likelihood that impactful resonance effects on Z_{DR} are seen only in data from higher-frequency systems (X and C band).

However, there still were several cases that were deemed unusable in this study, beyond the aforementioned criteria. The most common reason why cases could not be analyzed was because the algorithm connected the Z_{DR} column within a storm to an area of enhanced Z_{DR} associated with the melting layer (e.g., Fig. 5a). In such cases, using higher elevation angles often would bring the height of the analysis to well above 1 km

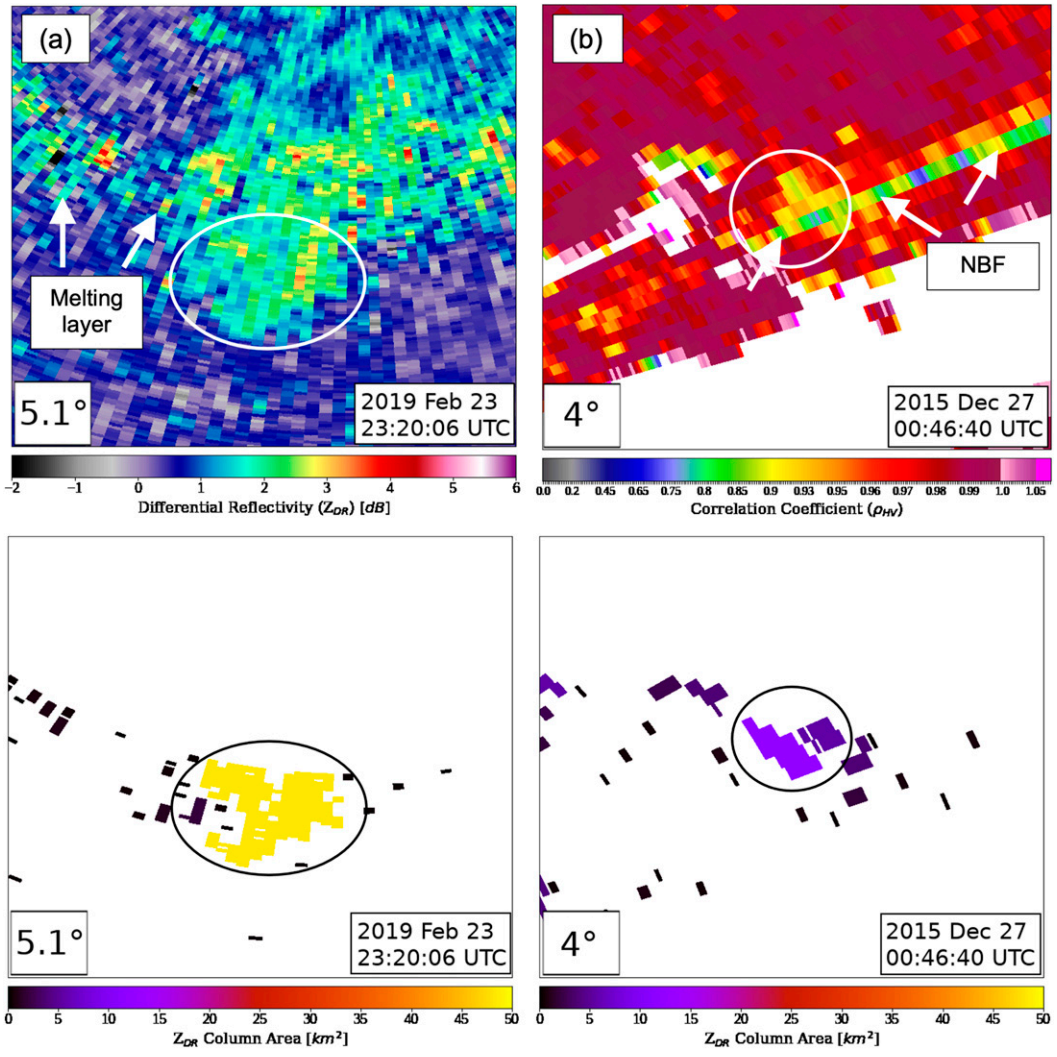

FIG. 5. Example cases that were not analyzed for this study owing to (a) melting layer interference for a tornadic supercell case on 23 Feb 2019 and (b) nonuniform beam filling for a tornadic supercell case on 27 Dec 2015. The top panel in (a) shows Z_{DR} (dB) and the bottom panel is Z_{DR} column area (km^2); the top panel of (b) shows the copolar correlation coefficient and the bottom panel is Z_{DR} column area (km^2). The circles enclose the most likely location of the Z_{DR} column in the opinion of the authors. The arrows in (a) denote enhanced areas of Z_{DR} in the melting layer, and in (b) areas of likely nonuniform beam filling.

above the 0°C level, and so those cases were not analyzed. A second common reason cases were not analyzed is the effects of artifacts in the data consistent with nonuniform beam filling (NBF; e.g., Fig. 5b), where reduced ρ_{HV} values led to the column area being reduced. Less frequently, there were multiple distinct columns without a clear indication of which was best associated with the supercell, or a noisy Z_{DR} field that made accurate identification of a Z_{DR} column too prone to large error to use in this study.

d. Statistical significance testing

The Wilcoxon rank sum test, a nonparametric test, is often used to provide statistical context to the results of two sets of data without assuming an underlying distribution. For our purposes, it is used to help quantify whether two sets of supercell Z_{DR} column area data derive from the same population distribution. In this study, the test uses a continuity correction. It also is directional for the intensity portion of the study because we know of no reason to expect that Z_{DR} column areas would be *smaller* for tornadic cases and *smaller* for stronger tornadoes (see section 3). The test is not directional for the tornadogenesis portion of the study. Statistical significance levels of 1% ($p \leq 0.01$) are emphasized. While the test is often stated as comparing the medians of two distributions, p values also are affected by spread when there are differences in the variances of two distributions (e.g., Hart 2001), as is the case in this study (see section 3a). Even small differences in spread, skewness, and sample size between two samples can

muddle interpretation of statistical tests when using most rank transformation approaches (Fagerland and Sandvik 2009). As a result, we encourage cautious interpretation of statistical tests herein and emphasize a holistic view of results. Also, in both sections, we provide the common language effect size (CLES; McGraw and Wong 1992), which gives the probability that a random value from one population will be greater than a random value from a second population. We used an improved version that does not assume a normal distribution and accounts for ties between pairs (Vargha and Delaney 2000).

3. Observations of Z_{DR} column areas

In this study, we used the development of an automated tool for Z_{DR} column area calculations to test two hypotheses about supercells:

1) Tornadic and nontornadic supercells exhibit substantial overlap in their Z_{DR} column areas at the time immediately prior to tornadogenesis and tornadogenesis failure, owing to the complicated multilayered nature of the tornadogenesis process.
2) Weakly tornadic supercells (EF1) exhibit significantly smaller Z_{DR} column areas than those in strong (EF2–3) and violent (EF4+) tornadoes at the time just prior to and at the time of tornadogenesis.

a. Tornadogenesis

In this section, the Z_{DR} column areas of tornadic and nontornadic supercells are compared. For nontornadic cases, instead of choosing a time at random for case analysis or averaging data from several times, we used the time of peak 0–1-km azimuthal shear (Mahalik et al. 2019) during the time each nontornadic case was within the 20–60-km range as the analysis time (e.g., Loeffler et al. 2020; Tuftedal et al. 2021). Based on previous work, and to accurately assess whether predictive[2] skill is supported, the cases were analyzed for the first volume in which the time of the scan used to estimate Z_{DR} column area occurs (i) after the tornado start time in *Storm Data* for tornadic cases and (ii) after the peak 0–1-km azimuthal shear in nontornadic cases; we refer to this volume as T. We also analyzed one volume prior to the T volume ($T-1$), which represents the first scan prior to tornado formation or peak 0–1-km azimuthal shear. The durations of WSR-88D volumes vary, so the time difference from estimated tornado onset to the time of the scan used to estimate Z_{DR} column area averaged +156 s (−153 s) for T ($T-1$) but was as large as +370 s (−386 s). We acknowledge inherent errors using estimated start times from *Storm Data* (e.g., Witt et al. 1998); cases with obvious low-level TVSs prior to this time were adjusted to the appropriate volume, but in practice this only amounted to a one-volume adjustment in a small subset of cases.

A comparison of all 107 tornadic and 30 nontornadic cases exhibiting Z_{DR} columns provides ostensibly strong evidence that tornadic supercells contain Z_{DR} column areas that are larger than those in nontornadic supercells imminently prior to tornadogenesis (Fig. 6a). The difference in mean (median) between tornadic [36 (31.4) km^2] and nontornadic cases [10.6 (7.6) km^2] is large, though there are still a number of tornadic cases that contain small (<20 km^2) areas. A hypothesis that the two sets of cases derive from the same distribution can be rejected at the 1% level, though small p values are likely influenced by the much larger spread in the tornadic case distribution and the differing sample sizes. There are also two additional important caveats to these results: (i) the tornadic cases were not chosen at random, but designed to reach an approximately equal number of EF1–3 cases, and (ii) cases in which no organized Z_{DR} column (area > 1 km^2) could be identified were not included.

To address the first caveat, the EF1 cases, the weakest surveyed tornadoes in our sample were isolated and compared with the nontornadic cases (Fig. 6b). Again, while the Z_{DR} column areas in EF1 cases are generally less than that in the whole set of tornadic cases, these results also are evidence of different underlying distributions. To address the second caveat, cases in which there was no identifiable Z_{DR} column or one with an area less than 1 km^2 were included, again for all tornadic and all nontornadic cases (Fig. 6c). The introduction of "no-column" cases brings the median value for tornadic cases down substantially (no-column prevalence in supercells is discussed in section 3b). The tornadic cases still comprise a distribution of areas much larger than that for the nontornadic cases though subject to the same variance influences. Finally, we address both caveats simultaneously, so that nontornadic cases are compared to only EF1 tornadic cases, including no-column cases in both sets (Fig. 6d). In this case, the hypothesis that the two underlying distributions are the same cannot be rejected. However, all 11 observations of large (i.e., >40 km^2) areas occur in EF1 cases.

The same analysis was run for one volume later, the first volume in which the relevant Z_{DR} column scan used occurred after the estimated time of tornadogenesis (Fig. 7). The results are very similar to that using the $T-1$ volume, and evidence of substantial separation between the distributions of areas for the two sets of cases (Figs. 7a–c). But again, when comparing nontornadic cases to EF1 cases and including no-column cases, the separation is substantially reduced (Fig. 7d). The similarity in area distributions between $T-1$ and T volumes is evidence that there are not large organized changes in Z_{DR} column areas leading up to the time of tornadogenesis or peak 0–1-km azimuthal shear.

One additional shortcoming of this study is the use of the EF scale to estimate tornado intensity. As already discussed, the most prominent downside of such an approach is the near certainty that some tornadoes will be underrated in intensity if they occur over open land; recent work has demonstrated that this effect is likely large (Wurman et al. 2021). Another approach,

[2] This study does not address whether Z_{DR} column areas provide a real-time *assessment* of *current* tornado intensity. In addition to the possibility of tornadic debris contamination of Z_{DR} for ongoing tornadoes, the mechanisms hypothesized in T17 necessarily require a time lag. In addition, a number of studies discussed in section 2 have already established more direct methods to estimate ongoing tornado intensity.

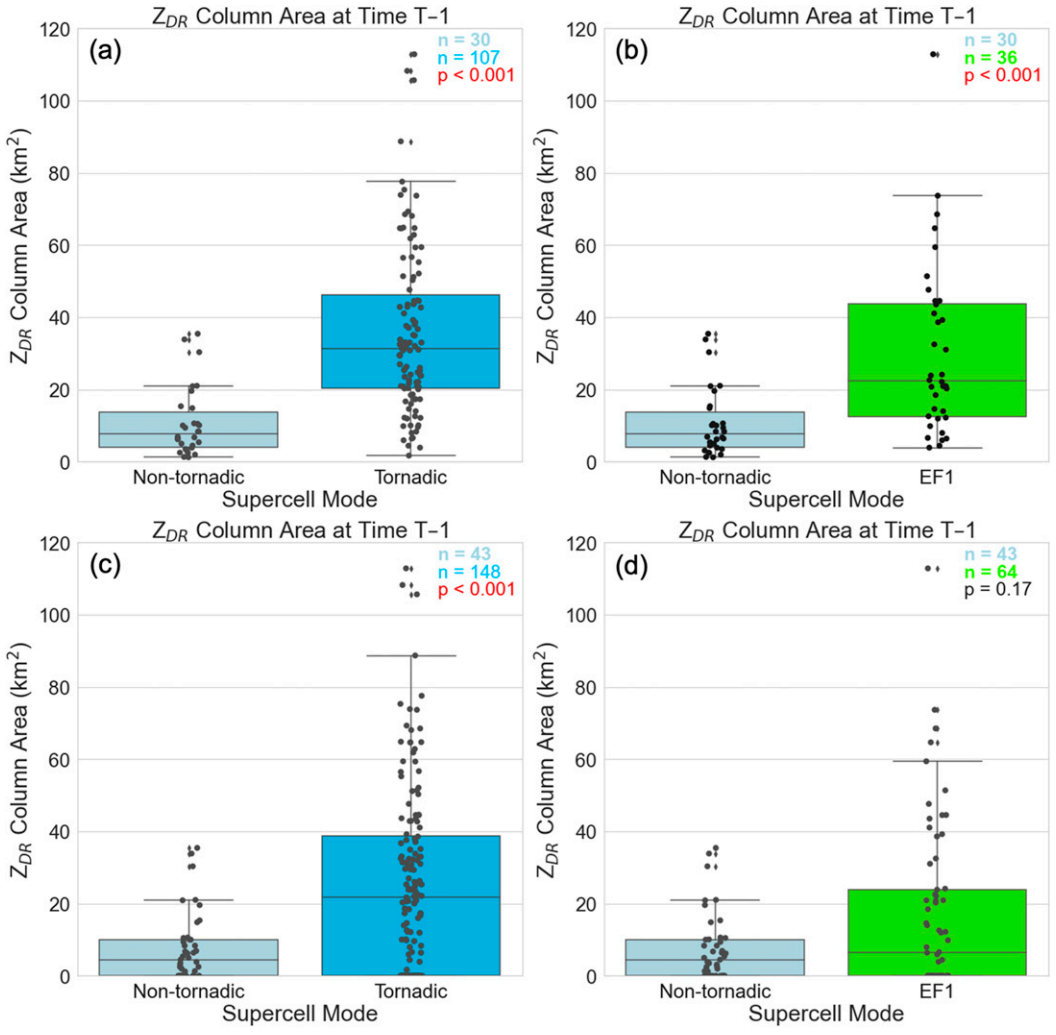

FIG. 6. Box-and-whisker plots comparing Z_{DR} column areas (km^2) of (a) nontornadic cases and tornadic cases with a Z_{DR} column, (b) nontornadic cases and EF1 cases with a Z_{DR} column, (c) all nontornadic cases and tornadic cases, and (d) all nontornadic cases and EF1 cases. All comparisons use data from the first Z_{DR} column scan prior to the tornadogenesis time in *Storm Data* or the time of peak 0–1-km azimuthal shear. The box encloses the 25th–75th data percentiles, the thin black line marks the median, and the whiskers encompass the rest of the values unless they are more than 1.5 times removed from the interquartile range, in which case they are plotted as outliers. Color-coded sample sizes and the p value for rejecting the hypothesis that both sets of data derive from the same underlying population appear in the top-right corner. The common language effect sizes for the right-hand column being larger than the left-hand column are 0.87 in (a), 0.81 in (b), 0.70 in (c), and 0.55 in (d).

albeit also imperfect (e.g., Snyder and Bluestein 2014), is to use peak TVS ΔV in WSR-88D radial velocity data to estimate tornado intensity. For the tornadic cases with Z_{DR} columns, the entirety of the tornado life cycle was manually examined and the peak ΔV recorded.[3] We compared nontornadic cases to the 30 tornadic cases with Z_{DR} columns at time $T - 1$ that had the *weakest* peak ΔV (Fig. 8). There is a distinction between the two sets of cases: a mean/median of 10.6/7.6 (20.8/25.8) km^2 for the nontornadic (weakly tornadic) cases. Therefore, in the cases sampled for this study, conditioned on there being a measurable Z_{DR} column, tornadic cases, even weakly tornadic cases, have somewhat larger and more variable Z_{DR} column areas than nontornadic cases in the time just prior to tornadogenesis or tornadogenesis failure.

Examples of a nontornadic and tornadic case with Z_{DR} column areas closest to the medians in Fig. 6a are shown (Fig. 9). The tornadic case (EF1) has a relatively large Z_{DR} column summed area of 31.4 km^2 (Fig. 9a) made up of three

[3] For ~10 cases, peak ΔV could not be reliably calculated, typically because there was not a definitive TVS identified in two consecutive volumes, and we believe potential errors to be too high using one TVS observation as indicative of peak TVS intensity.

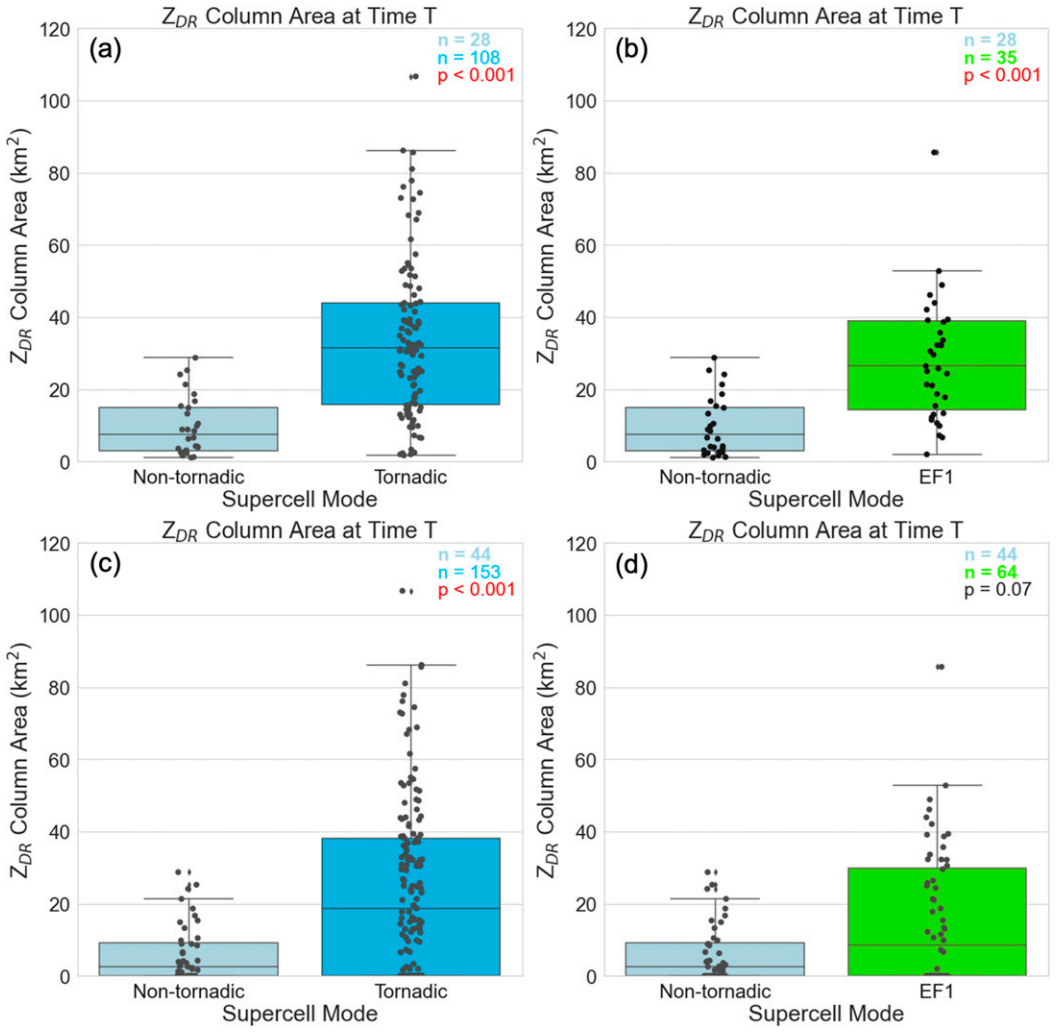

FIG. 7. As in Fig. 6, but all comparisons use data from the first Z_{DR} column scan after the tornadogenesis time in *Storm Data* or the time of peak 0–1-km azimuthal shear. The common language effect sizes are 0.87 in (a), 0.86 in (b), 0.70 in (c), and 0.58 in (d).

individual adjacent areas. This case was representative of most cases in which there was separation between the enhanced Z_{DR} associated with the column and that associated with the melting layer (red arrows in Fig. 9). The nontornadic case, in contrast, has a much smaller column area of 6.9 km^2 (Fig. 9b) made up of only one area, though again displaced from the area likely representative of the melting layer.

b. *Tornado intensity*

We now use our novel algorithm to compare the Z_{DR} column areas among 153 tornadoes of different surveyed EF scale ratings. The times analyzed, $T-1$ and T, are the same as those discussed in section 3a. The mean and median range of the Z_{DR} column observations increased with EF scale given the need to look at farther ranges to collect sufficient numbers of the relatively rare EF3+ cases. Cases at farther ranges use lower elevation angles, and therefore more horizontally oriented slices to get to the appropriate height level, in addition to the case radar gates being larger. Pearson correlation coefficients between range and Z_{DR} column area indicated either no or weak linear relationships: EF1 (0.04), EF2 (0.28), EF3 (0.31), and EF4 (0.17); correlations were much smaller when including no-column cases. Regardless, we cannot rule out minor range impacts on calculated areas.

The Z_{DR} column areas for the 108 tornadic cases in which the supercell in question had an identifiable Z_{DR} column at time T are separated by EF scale and compared (Fig. 10a). There is a clear separation in Z_{DR} column areas between the EF1–2 tornado cases (smaller areas) and the EF3+ tornado cases (larger areas). However, the distribution spreads are large on all Z_{DR} column areas, especially EF3 cases, in which the 25th–75th percentiles encompass values from ~30 to 70 km^2. There also is almost no separation between the areas of the weakest surveyed sets of tornadoes, EF1 (median of 26.5 km^2) and EF2 (median of 24.1 km^2). Statistical testing was performed in a variety of ways

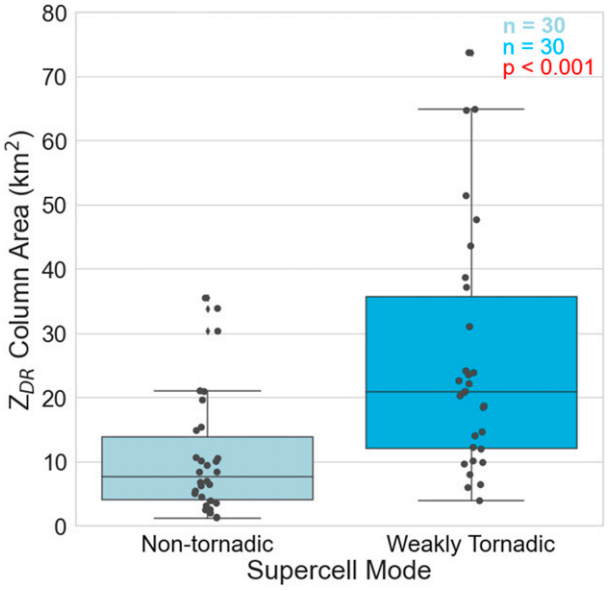

FIG. 8. As in Fig. 6, but comparing the Z_{DR} column areas of nontornadic cases and the 30 tornadic cases with the weakest peak ΔV in the TVS associated with the tornado. The common language effect size is 0.8.

to add context to the results. A hypothesis that the distributions come from the same underlying populations can be rejected at the 1% level for: EF3 versus EF1 cases, EF3 versus EF2 cases, and EF3+ versus EF1/2 cases. However, that same hypothesis cannot be rejected in this dataset for EF2 versus EF1 cases. The general pattern of distributions was similar when including cases in which no Z_{DR} column was identified (Fig. 10b): the EF3+ cases are much more likely to have large areas (>40 km^2) than the EF1–2 cases and we can reject hypotheses of the same underlying populations for the same sets as above. The inclusion of no-column cases reduces the EF1 median value to lower than that for EF2 cases, but there are not significant differences between the two sets.

The same data were analyzed, but for one volume scan prior, at time $T - 1$. A comparison of cases only with Z_{DR} columns (Fig. 10c) and including no-column cases (Fig. 10d) lead to similar results. In both cases, p values of <0.01 provide statistical support for the distributions of EF3+ cases being significantly different and resulting from different populations compared to EF1/2 cases, just as they were for time T. For the full set of cases in particular (Fig. 10d), (i) there is greater separation among all four sets of cases at time $T - 1$ compared to time T and (ii) the larger areas in the EF2 cases compared to EF1 cases is significant at the 5% level, but not the 1% level. Overall, the results of Fig. 10 and the accompanying statistical tests are significant evidence that supercells with larger Z_{DR} columns at or just after tornadogenesis tend to be more intense than those with smaller Z_{DR} columns, consistent with similar proxy work in Marion et al. (2019) and Sessa and Trapp (2020).

As discussed in section 3a, the use of the EF damage scale for tornado intensity is likely to strongly underestimate true near-ground tornado intensity. As a result, we next evaluate tornado intensity by using the peak ΔV measured at the lowest observed radar level for each case in which (i) there was a Z_{DR} column identified at time T and (ii) a TVS was identified in at least two separate volume scans (n = 98; Fig. 11a). There is a weak positive linear correlation (0.32) between peak ΔV and Z_{DR} column area, though with several outliers. A Spearman rank correlation, which is less sensitive to such outliers, is higher at 0.44. We also divided the 98 cases into thirds by their peak ΔV value and compared the Z_{DR} column areas at time T (Fig. 11b). The weakest two ΔV groups have a similar distribution of Z_{DR} column areas, and the distribution of cases with the strongest peak ΔV have statistically larger areas than the weak and moderate cases; these results somewhat mirror the EF case results seen in Figs. 10a,b. The same analysis was conducted for the $T - 1$ volume data (Figs. 11c,d), and the plots exhibit similar trends as those seen for time T. However, there is more separation between weak and moderate cases at time $T - 1$, which again mirrors the greater separation between EF1 and EF2 cases seen in Figs. 10c,d; the moderate case distribution is larger than the small case distribution at the 5% level but not the 1% level.

Examples of tornadic cases with Z_{DR} column areas closest to the medians in Fig. 10d are shown (Fig. 12). As surveyed intensity of the tornadoes increases from EF1 (Fig. 12a) to EF2 (Fig. 12b) to EF3 (Fig. 12c) to EF4 (Fig. 12d), so does the median-case Z_{DR} column area approximated by the algorithm, from 6.4 to 20.4 to 33.8 to 56.7 km^2, respectively.

Finally, we can use our data to estimate how prevalent a lack of an identifiable Z_{DR} column is in our sets of cases. However, using only the cases shown in Figs. 7 and 10 could be misleading because of the cases that did contain Z_{DR} columns but were precluded from analysis because of the other data quality issues discussed in section 2c. Once accounting for all cases that had a Z_{DR} column but were excluded for other reasons (Table 1), 16/54 (30%) of nontornadic cases and 45/220 tornadic cases (20%) lacked a Z_{DR} column. However, again the overall tornadic versus nontornadic sample is skewed because the presence of a Z_{DR} column also has a clear dependance on peak surveyed tornado intensity. Tornadoes rated EF3+ not only have larger Z_{DR} column areas, but they also are far less likely to lack a Z_{DR} column (8% of cases) than nontornadic or weakly tornadic (33%) cases at time T. So while there is little evidence to support large differences in Z_{DR} column prevalence between weakly tornadic and nontornadic cases, there is an indication that a lack of a Z_{DR} column may be associated with a lower chance of imminent formation of tornadoes rated EF3+.

4. Summary and discussion

Results from a large sample of tornadic and nontornadic supercells provide some evidence in support of both of our hypotheses, but with caveats. A polarimetric radar data proxy for the midlevel updraft area, the Z_{DR} column area ~1 km above the 0°C level, may be used at and just before tornado formation to differentiate weaker tornadoes from stronger tornadoes based on surveyed intensity. In addition, we find that nontornadic cases contain Z_{DR} column areas that are similar to but less variable than those from supercells producing EF1

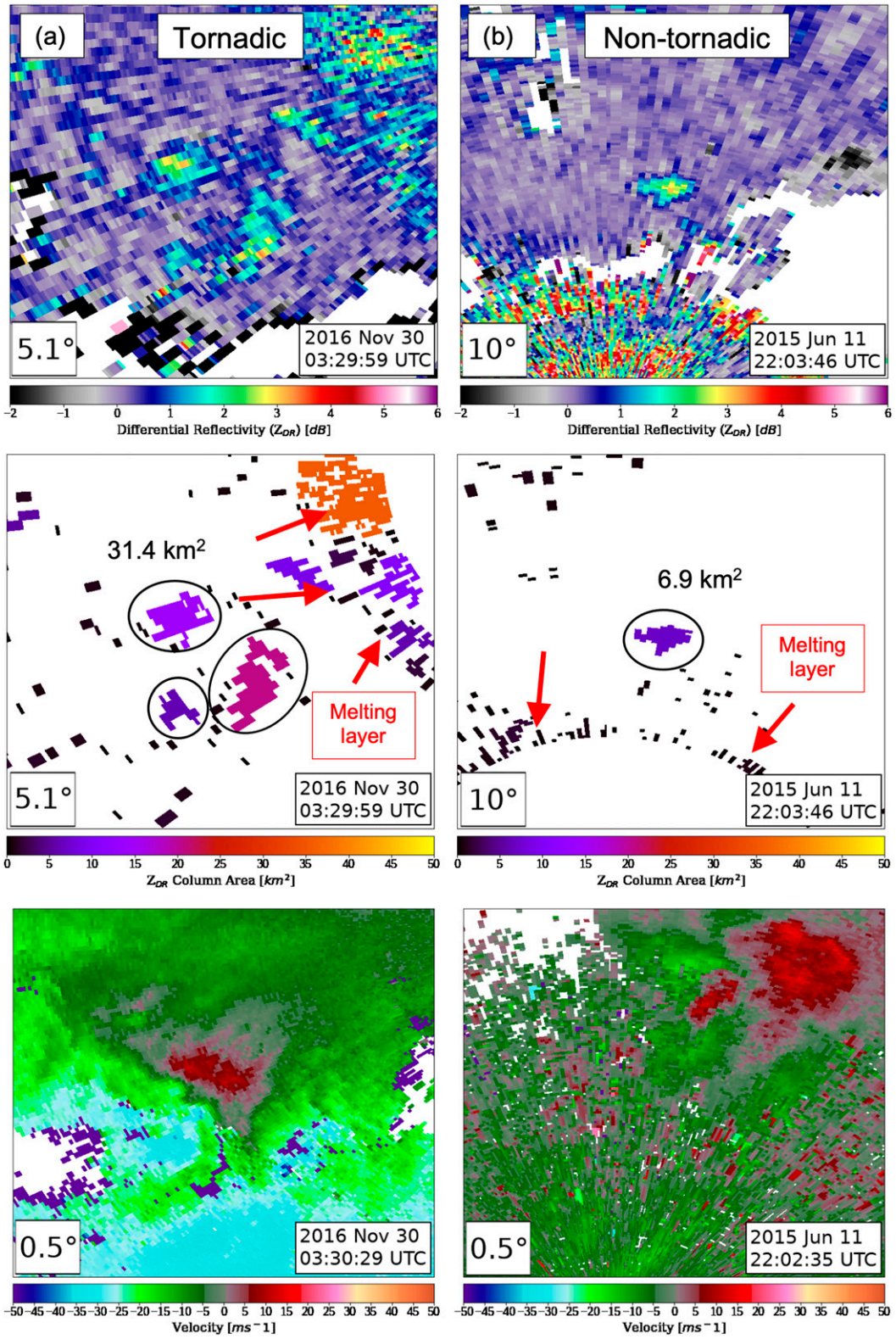

FIG. 9. Example of (a) a tornadic case from 30 Nov 2016 and (b) a nontornadic case from 11 Jun 2015, both examined in this study. For each case, shown are (top) Z_{DR} (dB), (middle) the modified TRENDSS Z_{DR} column area output (km^2), and (bottom) the 0.5° radial velocity (m s^{-1}) at genesis and genesis failure time. The summed column areas are shown for the three individual areas used in (a) and the one area used in (b), all of which are enclosed by circles. The red arrows point to areas likely marking the melting layer.

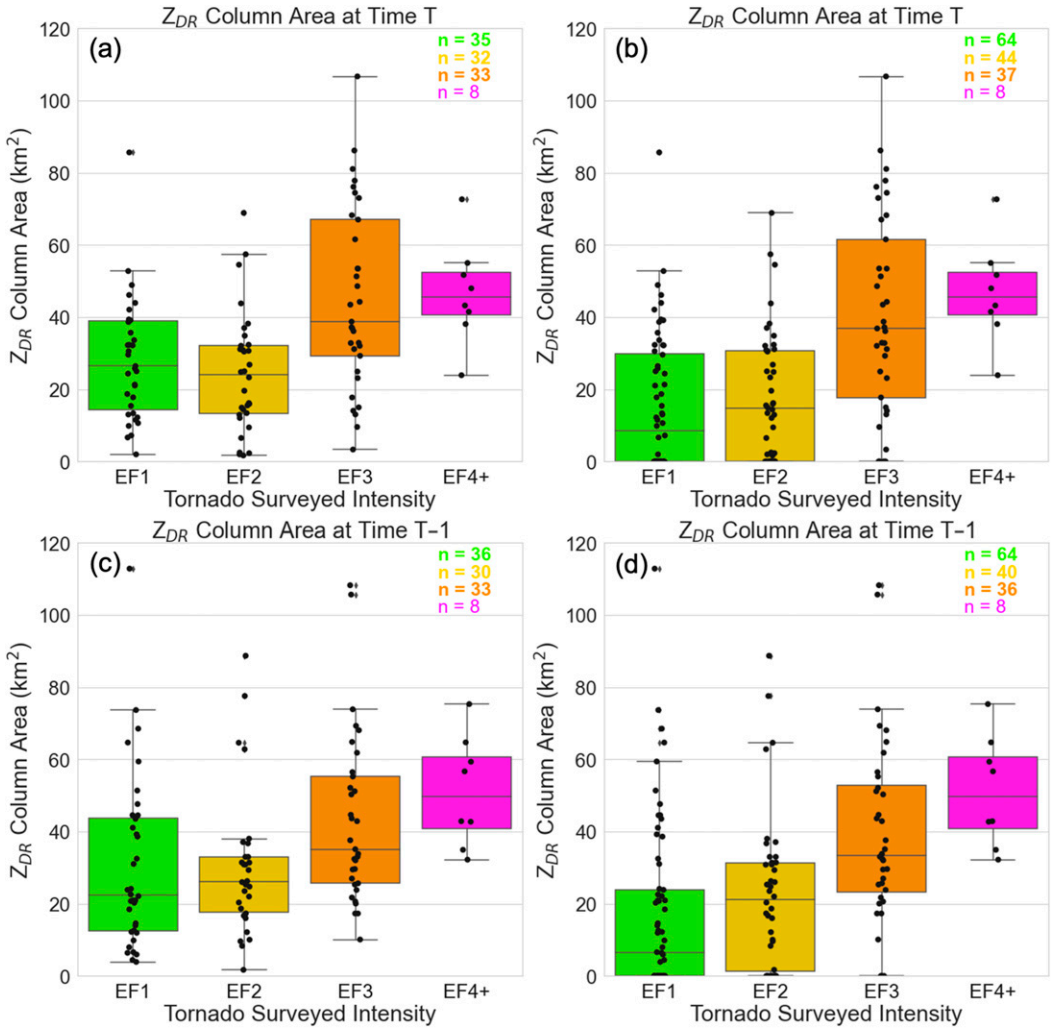

FIG. 10. Box-and-whisker plots comparing Z_{DR} column areas (km^2) of (a) tornadic cases with a Z_{DR} column at time T, (b) all tornadic cases at time T, (c) tornadic cases with a Z_{DR} column at time $T-1$, and (d) all tornadic cases at time $T-1$. Color-coded sample sizes appear in the top-right corner. The mean distance from the radar to the tornado is 41, 43, 63, and 73 km for the set of cases with tornadoes rated EF1, EF2, EF3, and EF4, respectively. The common language effect sizes for EF1/2 vs EF3+ cases are (a) 0.74, (b) 0.78, (c) 0.71, and (d) 0.77, respectively.

tornadoes. Also, the probability of there not being a Z_{DR} column at the time of tornadogenesis decreases with increasing surveyed tornado intensity, but is similar between nontornadic and weakly tornadic cases.

The first result is largely consistent with recent results. The theoretical work of T17 combined with this study and three previous observational studies (Van Den Broeke 2017; Marion et al. 2019; Sessa and Trapp 2020), all with distinct techniques to estimate updraft/mesocyclone size, provides strong evidence that the relationship between updraft size and tornado intensity hypothesized in T17 is real and robust. One difference in this study is that the relationship between Z_{DR} column area and radar-estimated tornado intensity is not as strong as presented in the aforementioned studies. This may be a function of the different features, as each case analyzed in Marion et al. (2019) and Sessa and Trapp (2020) identified the updraft proxy (an OT or mesocyclone, respectively), whereas not every case in this study had a Z_{DR} column despite the supercell, by definition, having an updraft. In addition, this study did not examine EF0 cases, which mitigated underrate bias concerns, but also likely leaves out the weakest tornadoes, which may otherwise enhance correlations. This study also did not average updraft size data over several time periods as in some other studies.

We have not thus far described efforts to determine if *mechanisms* hypothesized to be responsible for the link between updraft width and tornado intensity in past studies are supported in this study. One possibility is to analyze estimated tornado path widths. Part of the T17 hypothesis is that the larger updraft/mesocyclone leads to tornadoes that are wider, which have previously been shown to have higher tornado damage intensity (Brooks 2004). And Sessa and Trapp (2020)

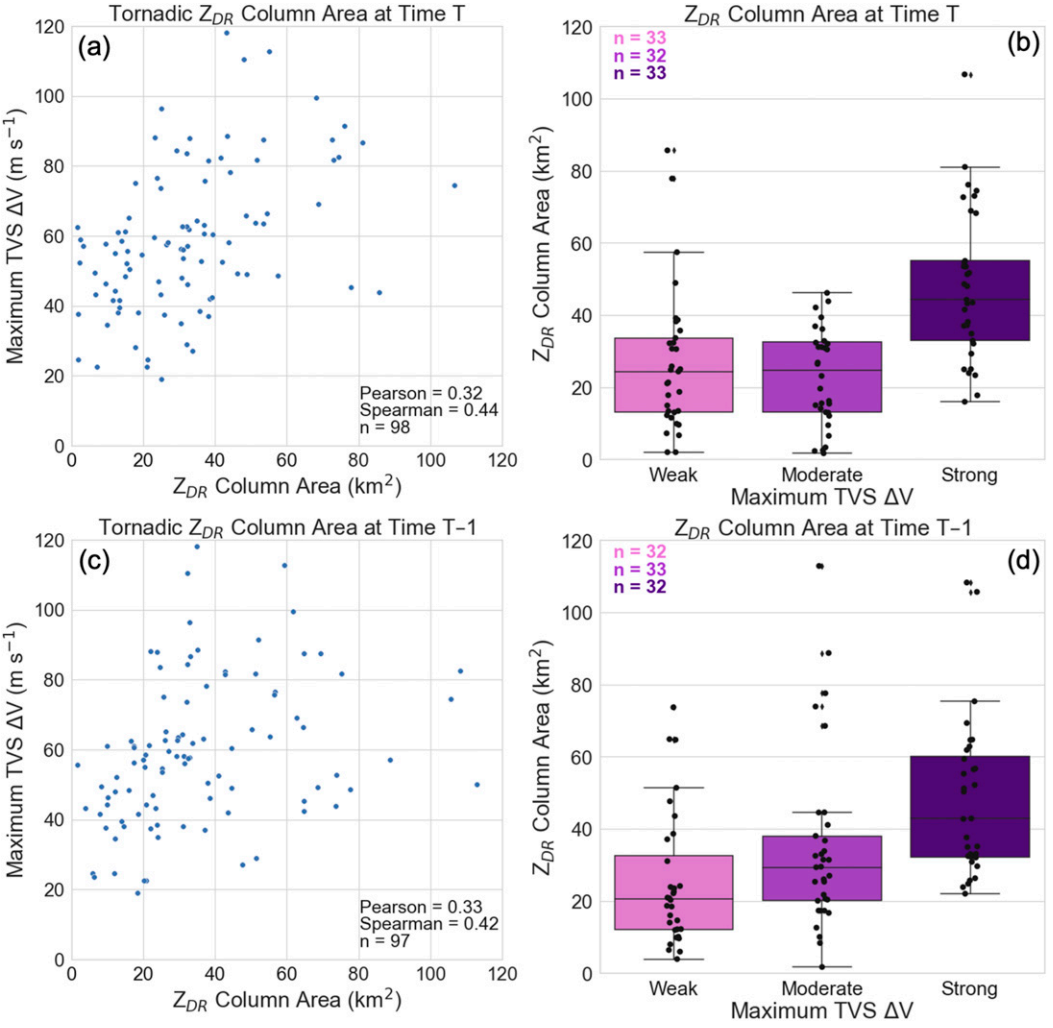

FIG. 11. Comparisons of Z_{DR} column areas with radar-estimated peak tornado intensity. (a),(c) Scatterplots of Z_{DR} column area (km^2) vs maximum ΔV in the TVS associated with the tornado at times T and $T-1$, respectively, and (b),(d) box-and-whisker plots of Z_{DR} column area in evenly divided thirds of maximum ΔV in the TVS associated with the tornado at times T and $T-1$, respectively. For (a) and (c), the Pearson and Spearman correlation coefficients appear at the bottom right and for all plots, and sample sizes are provided. The common language effect sizes for weak vs strong cases are 0.8 in (b) and 0.82 in (d).

found evidence that this relationship held in their analysis of 40 supercell cases (see their Fig. 17). For the subset of tornadic cases that contained information about peak tornado width, we compared the recorded values with updraft area at time T (Fig. 13a). In this case, there is a lack of linear signal, either using Pearson (0.13) or Spearman (0.16) correlation coefficients. Dividing cases into bins of peak surveyed widths of <500, 500–1000, and 1000+ yd and comparing Z_{DR} column areas provides some separation for the latter category, albeit with a very small number of cases (Fig. 13b), and a hypothesis that the distributions are the same cannot be rejected. The same general relationships hold for time $T-1$ (not shown).

What do we make of this discrepancy? It may be that there is a more direct relationship between low-level mesocyclone width and tornado width than there is with midlevel updraft width given the hypothesized mechanisms in T17. However, we also consider the likely large error bars inherent in using damage to estimate tornado diameter. In fact, we question if such a relationship has the support of strong evidence, especially in light of recent work. Wurman et al. (2021) show that there is essentially no relationship between radar-derived estimates of tornado width and radar-derived intensity estimates (see their Fig. 4), which provides additional uncertainty about the pathways hypothesized in T17. So while our results are broadly consistent with what is hypothesized in T17, we lack sufficient data to attach the results to the T17 mechanisms.

The latter results introduce a number of additional questions that motivate future work. The past observational studies that have quantified estimates of supercell updraft

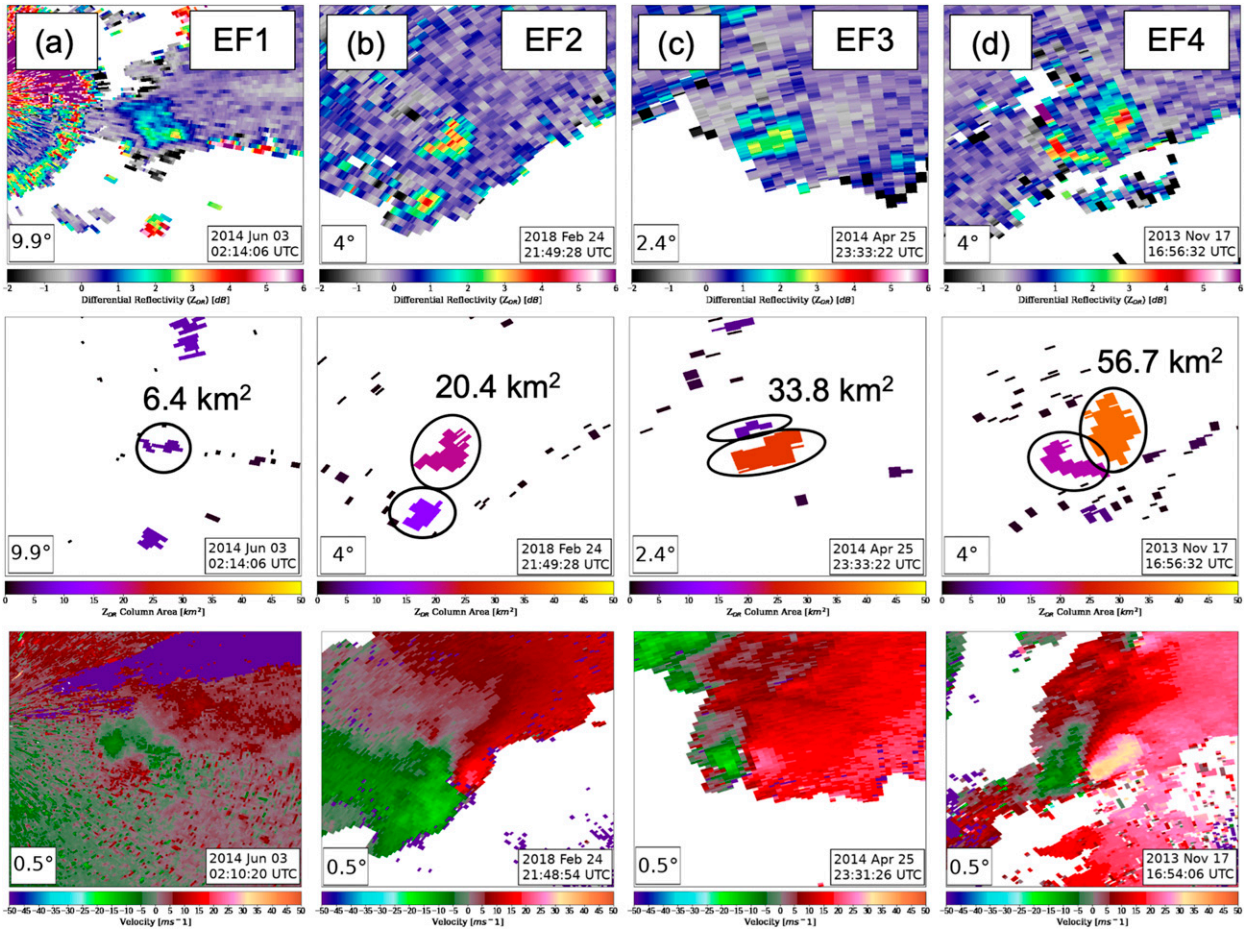

FIG. 12. As in Fig. 9, but for tornadic cases rated (a) EF1 from 4 Jun 2014, (b) EF2 from 24 Feb 2018, (c) EF3 from 25 Apr 2014, and (d) EF4 from 17 Nov 2013.

size in a rigorous manner, Marion et al. (2019) and Sessa and Trapp (2020), did not examine nontornadic cases. T17 did comment that their ideas also could be related to tornadogenesis when tornadoes result from contraction of a mesocyclone. However, evidence of the ubiquity of ''bottom-up'' tornadogenesis (e.g., French et al. 2013), and the focus of recent literature on (i) the importance of processes like dynamic lifting on low-level mesocyclone development (e.g., Markowski and Richardson 2014; Coffer and Parker 2017), and (ii) the link between very near-ground environmental conditions and tornadogenesis (e.g., 0–500-m SRH; Coffer et al. 2019), may belie such a process. In addition, the T17 mechanism is likely to require a time lag (Trapp et al. 2018) while we investigated Z_{DR} column area just prior to tornadogenesis.

Another possibility we consider is how the near-storm environment (NSE) may link updraft area to both tornadogenesis and peak tornado intensity. Both Warren et al. (2017) and Peters et al. (2019) found in simulation studies that larger updraft area results from stronger deep-layer vertical wind shear that enhance storm motions and storm-relative low-level flow (this can also be seen in other simulation data, for example, from Coffer and Markowski 2018). Peters et al. (2020) deconstructed the role of SRH in a combined proximity sounding and simulation study,

TABLE 1. Contingency table of Z_{DR} column identification for nontornadic supercell cases, and supercells that produced tornadoes rated EF1, EF2, EF3, and EF4+ at time T.

	Survey					
Column?	NT	EF1	EF2	EF3	EF4+	Total
Yes	38 (70%)	61 (67%)	65 (84%)	41 (91%)	8 (100%)	213 (78%)
No	16 (30%)	29 (33%)	12 (16%)	4 (9%)	0 (0%)	61 (22%)
Total	54	90	77	45	8	274

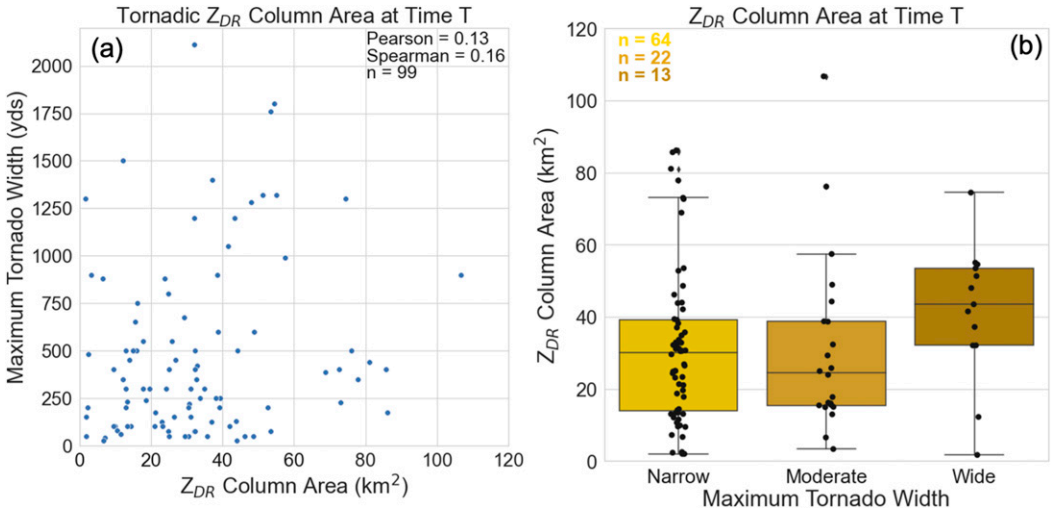

FIG. 13. Comparisons of Z_{DR} column areas with surveyed peak tornado width. (a) Scatterplot of Z_{DR} column area (km^2) vs maximum surveyed tornado width at time T, and (b) box-and-whisker plots comparing Z_{DR} column area for narrow (<500 yd), moderate (500–1000 yd), and wide (>1000 yd) surveyed tornadoes at time T. For (a), the Pearson and Spearman correlation coefficients appear at the top right and the sample sizes are provided in both (a) and (b).

finding that the most relevant part of SRH for low-level rotation is streamwise vorticity while storm-relative flow is more important for, among other quantities, supercell storm mode and updraft area. Based on these studies, work is ongoing using the modified TRENDSS algorithm, WSR-88D radial velocity data, and NSE data to determine if the relationship among midlevel updraft area, low-level mesocyclone area, and tornado formation and intensity can be explained through shared environmental pathways. May, for example, strong tornadoes and large midlevel updrafts be correlated through their mutual relationship to large SRH (i.e., streamwise vorticity for tornadoes and SR flow for updraft area)? We hope these efforts and others help to clarify the mechanisms responsible for linkages found in this study and previous works.

Finally, based on study results, we issue the following preliminary guidelines to forecasters:

- for a supercell not currently producing a tornado, if the radar volume does not contain a Z_{DR} column or has a small Z_{DR} column (<10 km^2) within two elevation angle scans of the 0°C level, there is a low risk of imminent EF3+ tornado formation;
- for a supercell not currently producing a tornado, if the radar volume contains a Z_{DR} column with an area > 40 km^2 within two elevation angle scans of the 0°C level, there is an increased risk of imminent tornado formation compared to a situation in which column area < 40 km^2;
- once a supercell tornado has formed, if the corresponding radar tornadogenesis volume does not contain an identifiable Z_{DR} column or has a small Z_{DR} column (<10 km^2) within two elevation angle scans of the 0°C level, there is a low risk of the tornado reaching EF3+ intensity; and
- once a supercell tornado has formed, if the corresponding radar tornadogenesis volume contains a Z_{DR} column with an area >40 km^2 within two elevation angle scans of the 0°C level, there is an increased risk of the tornado reaching EF3+ intensity compared to a situation in which the column area < 40 km^2.

Despite some apparent differences in the column areas of tornadic and nontornadic supercells, we believe the utility of Z_{DR} column areas in tornadogenesis forecasting overall to be highly conditional, which can be seen in our guidelines (i.e., both EF3+ tornadoes and 40+ km^2 areas are rare events). We only recommend its use in concert with all relevant forecasting information because of the small separation of areas between nontornadic cases and weakly tornadic cases (Fig. 6d). In addition, we lack a satisfactory mechanism with evidence to explain updraft areal differences between tornadic and nontornadic cases. Similarly, for peak intensity, the unrepresentative tornado intensity sample used in this study means that even though a large percentage of EF3+ cases have large column areas, the overall low relative frequency of EF3+ cases means that there would be a large number of false alarms if large column areas were used without putting the information in context of other relevant NWP and observational data. With a column area signal now firmly established, future work should take a more skill-score-oriented approach to its use. In addition, though we analyzed a large number of cases, our focus was establishing an overall link and we did not examine potential regional differences, such as those that may result from the impact of differing common NSEs.

The guidelines assume a forecaster has the ability to estimate Z_{DR} column area in real time. We believe the immunity to Z_{DR} bias and the partially automated detection and area calculation in the modified TRENDSS algorithm makes it an attractive option for real-time operational use. Drawbacks include the use of modeled estimates of the 0°C height level, melting layer

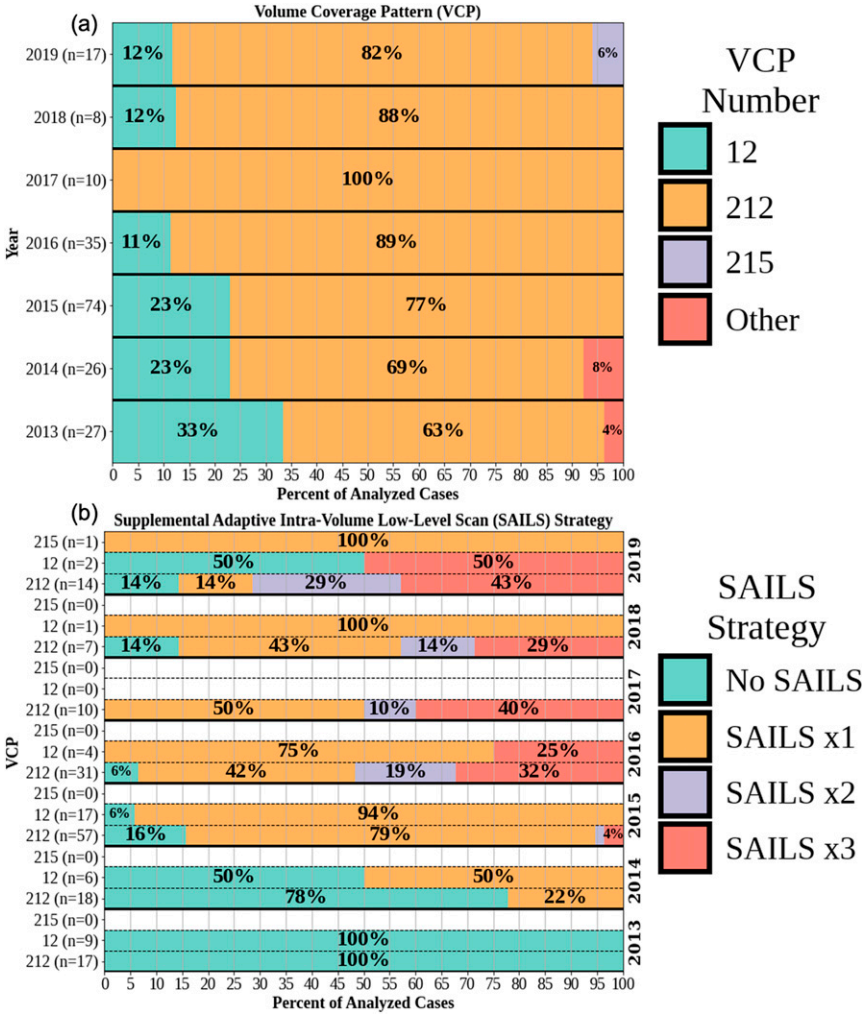

FIG. 14. Bar graphs showing annual trends in radar scanning patterns usage for the cases analyzed in this study. (a) VCP usage and (b) SAILS version usage for VCP 12, 212, and 215.

intrusion or NBF, potential difficulty of updraft isolation when rapid cyclic tornadogenesis is occurring, and some subjectivity involved in determining which area "clusters" belong to the Z_{DR} column. Also, viability for usage at long ranges is unknown, though there were no obvious issues implementing the algorithm for the EF3+ cases that occurred at 60–100-km range and, because the Z_{DR} column occurs ~3+ km in height, we believe the algorithm should be operable at ranges beyond 100 km. Finally, broadly speaking, more work is needed to determine just how effectively Z_{DR} column area represents updraft area (i.e., what is the influence of vertical velocity on Z_{DR} column areas?).

In addition, one also may wonder about the applicability of our results to QLCS mesocyclonic tornadoes. Marion et al. (2019) and Sessa and Trapp (2020) found that updraft width was related to tornado intensity in QLCSs, but the signal in the latter study was weaker in QLCSs than in supercells. And recently, Marion and Trapp (2021) simulated tornadic-like vortices in QLCSs and found that low-level mesocyclone area was related to tornado intensity, but they cautioned that intensity also was modulated by other factors. Given these results and the relatively short life cycles and unsteady nature of updraft cores in Marion and Trapp (2021), we are not confident that an approach using Z_{DR} columns, which is a midlevel updraft proxy, would yield beneficial results operationally in QLCSs.

Another potential problem in using TRENDSS in real time is the continued increase in use of supplemental adaptive intravolume low-level scans (SAILS; Chrisman 2013) and multiple elevation scan option SAILS (MESO-SAILS; Daniel et al. 2014) in severe storm nowcasting, which increases the time between elevated scans that would likely be used to identify the Z_{DR} column. For volume coverage pattern (VCP) 212, this activation has increased total volume scanning times from 255 s with no SAILS to 290 s with SAILS, and up to 343 s with MESO-SAILS. For the 198 analyzed cases in our study, the VCP used by the radar was VCP 12 or 212 for 98% of cases (Fig. 14a). VCP 215 was added operationally in 2018 and was used in one case. The remaining three cases used VCP 21, VCP

121, and VCP 211. VCPs 12/212 supported the selection of SAILS since 2014 and MESO-SAILS since 2015 and VCP 215 supported SAILS only during the study period. In cases analyzed since 2015, 88% (127/144) of cases had a radar scanning with SAILS/MESO-SAILS activated (Fig. 14b). However, we believe the modified TRENDSS algorithm is very much usable under these circumstances given the results discussed in section 3, and their general lack of sensitivity to whether the T or $T-1$ volume was used. Nonetheless, other applications of storm updraft proxies that depend on frequent mid and upper-level supercell data and/or vertically coherent data collection may be negatively impacted by use of SAILS or MESO-SAILS.

We encourage continued work optimizing the best combinations of radar-based tools to nowcast tornadogenesis and intensity (e.g., Gibbs and Bowers 2019). In addition to having indirect confirmation of a relationship between midlevel updraft area and low-level mesocyclone width, having redundant radar nowcasting tools for tornado intensity prediction may be valuable given potential advantages and drawbacks of using midlevel data. Possible examples of the former include storms at great range from all radar origins and mesocyclones with variable or indeterminate width. Examples of the former include aforementioned issues of melting layer interference, NBF, and attenuation. There may be improved peak tornado intensity predictive capability using some combination of OTA, Z_{DR} column area, and low-level mesocyclone width that requires future work to optimize. All of these factors are in addition to near-storm environmental considerations and other remote sensing-based nowcasting techniques (e.g., Sandmæl et al. 2019; Loeffler et al. 2020; Smith et al. 2020b), which we believe may together provide robust prediction of tornado formation and peak tornado intensity.

Acknowledgments. We thank Kristofer Tuftedal (Stony Brook University) for help refining cases in an earlier version of this work and Gregory Dean for assisting with the data entry. Constructive comments from Geoffrey Marion (NSSL) and two anonymous reviewers greatly improved the focus of this article. This study was supported by NSF Grants AGS-1748177 (French) and AGS-1748191 (Kingfield).

Data availability statement. This study's data, radar data from WSR-88D, and tornado database information from *Storm Events* are available from the National Centers for Environmental Information (ncdc.noaa.gov). The output of algorithms and edited case data number several hundred cases when accounting for cases considered and eliminated. As a result, please contact either author for data access and information about how they can be viewed in WDSS-II.

REFERENCES

Alexander, C. R., 2010: A mobile radar based climatology of supercell tornado structure and dynamics. Ph.D. dissertation, University of Oklahoma, 229 pp., https://doi.org/11244/319059.

Benjamin, S. G., and Coauthors, 2016: A North American hourly assimilation and model forecast cycle: The Rapid Refresh. *Mon. Wea. Rev.*, **144**, 1669–1694, https://doi.org/10.1175/MWR-D-15-0242.1.

Bluestein, H. B., K. J. Thiem, J. C. Snyder, and J. B. Houser, 2018: The multiple-vortex structure of the El Reno, Oklahoma, tornado on 31 May 2013. *Mon. Wea. Rev.*, **146**, 2483–2502, https://doi.org/10.1175/MWR-D-18-0073.1.

Brandes, E. A., J. Vivekanandan, J. D. Tuttle, and C. J. Kessinger, 1995: A study of thunderstorm microphysics with multiparameter radar and aircraft observations. *Mon. Wea. Rev.*, **123**, 3129–3143, https://doi.org/10.1175/1520-0493(1995)123<3129:ASOTMW>2.0.CO;2.

Brooks, H. E., 2004: On the relationship of tornado path length and width to intensity. *Wea. Forecasting*, **19**, 310–319, https://doi.org/10.1175/1520-0434(2004)019<0310:OTROTP>2.0.CO;2.

Burgess, D. W., M. A. Magsig, J. Wurman, D. C. Dowell, and Y. Richardson, 2002: Radar observations of the 3 May 1999 Oklahoma City tornado. *Wea. Forecasting*, **17**, 456–471, https://doi.org/10.1175/1520-0434(2002)017<0456:ROTMO>2.0.CO;2.

Casteel, M. A., 2016: Communicating increased risk: An empirical investigation of the National Weather Service's impact-based warnings. *Wea. Climate Soc.*, **8**, 219–232, https://doi.org/10.1175/WCAS-D-15-0044.1.

Chrisman, J. N., 2013: Dynamic scanning. *NEXRAD Now*, No. 22, NOAA, 1–3, https://www.roc.noaa.gov/WSR88D/PublicDocs/NNOW/NNow22c.pdf.

Coffer, B. E., and M. D. Parker, 2017: Simulated supercells in nontornadic and tornadic VORTEX2 environments. *Mon. Wea. Rev.*, **145**, 149–180, https://doi.org/10.1175/MWR-D-16-0226.1.

——, and P. M. Markowski, 2018: Comments on "The regulation of tornado intensity by updraft width." *J. Atmos. Sci.*, **75**, 4049–4056, https://doi.org/10.1175/JAS-D-18-0170.1.

——, M. D. Parker, R. L. Thompson, B. T. Smith, and R. E. Jewell, 2019: Using near-ground storm relative helicity in supercell tornado forecasting. *Wea. Forecasting*, **34**, 1417–1435, https://doi.org/10.1175/WAF-D-19-0115.1.

Cohen, A. E., J. B. Cohen, R. L. Thompson, and B. T. Smith, 2018: Simulating tornado probability and tornado wind speed based on statistical models. *Wea. Forecasting*, **33**, 1099–1108, https://doi.org/10.1175/WAF-D-17-0170.1.

Conway, J. W., and D. S. Zrnić, 1993: A study of embryo production and hail growth using dual-Doppler and multiparameter radars. *Mon. Wea. Rev.*, **121**, 2511–2528, https://doi.org/10.1175/1520-0493(1993)121<2511:ASOEPA>2.0.CO;2.

Daniel, A. E., J. N. Chrisman, C. A. Ray, S. D. Smith, and M. W. Miller, 2014: New WSR-88D operational techniques: Responding to recent weather events. *30th Conf. on Environmental Information Processing Technologies*, Atlanta, GA, Amer. Meteor. Soc., 5.2, https://ams.confex.com/ams/94Annual/webprogram/Paper241216.html.

Dowell, D. C., and H. B. Bluestein, 2002: The 8 June 1995 McLean, Texas, storm. Part I: Observations of cyclic tornadogenesis. *Mon. Wea. Rev.*, **130**, 2626–2648, https://doi.org/10.1175/1520-0493(2002)130<2626:TJMTSP>2.0.CO;2.

Fagerland, M. W., and L. Sandvik, 2009: The Wilcoxon–Mann–Whitney test under scrutiny. *Stat. Med.*, **28**, 1487–1497, https://doi.org/10.1002/sim.3561.

Fischer, J., and J. M. L. Dahl, 2020: The relative importance of updraft and cold pool characteristics in supercell tornadogenesis using highly idealized simulations. *J. Atmos. Sci.*, **77**, 4089–4107, https://doi.org/10.1175/JAS-D-20-0126.1.

French, M. M., and D. M. Kingfield, 2019: Dissipation characteristics of tornadic vortex signatures associated with long-duration tornadoes. *J. Appl. Meteor. Climatol.*, **58**, 317–339, https://doi.org/10.1175/JAMC-D-18-0187.1.

——, H. B. Bluestein, I. PopStefanija, C. A. Baldi, and R. T. Bluth, 2013: Reexamining the vertical development of tornadic vortex signatures in supercells. *Mon. Wea. Rev.*, **141**, 4576–4601, https://doi.org/10.1175/MWR-D-12-00315.1.

——, ——, ——, C. Baldi, and R. T. Bluth, 2014: Mobile, phased-array, Doppler radar observations of tornadoes at X band. *Mon. Wea. Rev.*, **142**, 1010–1036, https://doi.org/10.1175/MWR-D-13-00101.1.

——, D. W. Burgess, E. R. Mansell, and L. J. Wicker, 2015: Bulk hook echo raindrop sizes retrieved using mobile, polarimetric Doppler radar observations. *J. Appl. Meteor. Climatol.*, **54**, 423–450, https://doi.org/10.1175/JAMC-D-14-0171.1.

Gibbs, J. G., 2016: A skill assessment of techniques for real-time diagnosis and short-term prediction of tornado intensity using the WSR-88D. *J. Oper. Meteor.*, **4**, 170–181, https://doi.org/10.15191/nwajom.2016.0413.

——, and B. R. Bowers, 2019: Techniques and thresholds of significance for using WSR-88D velocity data to anticipate significant tornadoes. *J. Oper. Meteor.*, **7**, 117–137, https://doi.org/10.15191/nwajom.2019.0709.

Goldacker, N. A., and M. D. Parker, 2021: Low-level updraft intensification in response to environmental wind profiles. *J. Atmos. Sci.*, **78**, 2763–2781, https://doi.org/10.1175/JAS-D-20-0354.1.

Griffin, C. B., D. J. Bodine, J. M. Kurdzo, A. Mahre, and R. D. Palmer, 2019: High-temporal resolution observations of the 27 May 2015 Canadian, Texas, tornado using the Atmospheric Imaging Radar. *Mon. Wea. Rev.*, **147**, 873–891, https://doi.org/10.1175/MWR-D-18-0297.1.

Hart, A., 2001: Mann–Whitney test is not just a test of medians: Differences in spread can be important. *BMJ*, **323**, 391–393, https://doi.org/10.1136/bmj.323.7309.391.

Homeyer, C. R., T. N. Sandmæl, C. K. Potvin, and A. M. Murphy, 2020: Distinguishing characteristics of tornadic and non-tornadic supercell storms from composite mean analyses of radar observations. *Mon. Wea. Rev.*, **148**, 5015–5040, https://doi.org/10.1175/MWR-D-20-0136.1.

Illingworth, A. J., J. W. F. Goddard, and S. M. Cherry, 1987: Polarization radar studies of precipitation development in convective storms. *Quart. J. Roy. Meteor. Soc.*, **113**, 469–489, https://doi.org/10.1002/qj.49711347604.

Kingfield, D. M., and J. G. LaDue, 2015: The relationship between automated low-level velocity calculations from the WSR-88D and maximum tornado intensity determined from damage surveys. *Wea. Forecasting*, **30**, 1125–1139, https://doi.org/10.1175/WAF-D-14-00096.1.

——, and J. C. Picca, 2018: Development of an operational convective nowcasting algorithm using raindrop size sorting information from polarimetric radar data. *Wea. Forecasting*, **33**, 1477–1495, https://doi.org/10.1175/WAF-D-18-0025.1.

Kirkpatrick, C., E. W. McCaul Jr., and C. Cohen, 2009: Variability of updraft and downdraft characteristics in a large parameter space study of convective storms. *Mon. Wea. Rev.*, **137**, 1550–1561, https://doi.org/10.1175/2008MWR2703.1.

Klees, A. M., Y. P. Richardson, P. M. Markowski, C. Weiss, J. M. Wurman, and K. K. Kosiba, 2016: Comparison of the tornadic and nontornadic supercells intercepted by VORTEX2 on 10 June 2010. *Mon. Wea. Rev.*, **144**, 3201–3231, https://doi.org/10.1175/MWR-D-15-0345.1.

Kumjian, M. R., and A. V. Ryzhkov, 2008a: Microphysical differences between tornadic and non-tornadic supercell rear-flank downdrafts revealed by dual-polarization radar measurements. *24th Conf. on Severe Local Storms*, Savannah, GA, Amer. Meteor. Soc., 3B.4, https://ams.confex.com/ams/24SLS/techprogram/paper_141912.htm.

——, and ——, 2008b: Polarimetric signatures in supercell thunderstorms. *J. Appl. Meteor. Climatol.*, **47**, 1940–1961, https://doi.org/10.1175/2007JAMC1874.1.

——, ——, V. M. Melnikov, and T. J. Schuur, 2010: Rapid-scan super-resolution observations of a cyclic supercell with a dual-polarization WSR-88D. *Mon. Wea. Rev.*, **138**, 3762–3786, https://doi.org/10.1175/2010MWR3322.1.

——, A. P. Khain, N. Benmoshe, E. Ilotoviz, A. V. Ryzhkov, and V. T. J. Phillips, 2014: The anatomy and physics of Z_{DR} columns: Investigating a polarimetric radar signature with a spectral bin microphysical model. *J. Appl. Meteor. Climatol.*, **53**, 1820–1843, https://doi.org/10.1175/JAMC-D-13-0354.1.

Kuster, C. M., J. C. Snyder, T. J. Schuur, T. T. Lindley, P. L. Heinselman, J. C. Furtado, J. W. Brogden, and R. Toomey, 2019: Rapid-update radar observations of Z_{DR} column depth and its use in the warning decision process. *Wea. Forecasting*, **34**, 1173–1188, https://doi.org/10.1175/WAF-D-19-0024.1.

Lakshmanan, V., 2012: *Automating the Analysis of Spatial Grids: A Practical Guide to Data Mining Geospatial Images for Human and Environmental Applications*. Springer, 320 pp., https://doi.org/10.1007/978-94-007-4075-4.

Loeffler, S. D., M. R. Kumjian, M. Jurewicz, and M. M. French, 2020: Differentiating between tornadic and nontornadic supercells using polarimetric radar signatures of hydrometeor size sorting. *Geophys. Res. Lett.*, **47**, e2020GL088242, https://doi.org/10.1029/2020GL088242.

Loney, M. L., D. S. Zrnić, J. M. Straka, and A. V. Ryzhkov, 2002: Enhanced polarimetric radar signatures above the melting level in a supercell storm. *J. Appl. Meteor.*, **41**, 1179–1194, https://doi.org/10.1175/1520-0450(2002)041<1179:EPRSAT>2.0.CO;2.

Mahalik, M. C., B. R. Smith, K. L. Elmore, D. M. Kingfield, K. L. Ortega, and T. M. Smith, 2019: Estimates of gradients in radar moments using a linear least squares derivative technique. *Wea. Forecasting*, **34**, 415–434, https://doi.org/10.1175/WAF-D-18-0095.1.

Marion, G. R., and R. J. Trapp, 2021: Controls of quasi-linear convective system tornado intensity. *J. Atmos. Sci.*, **78**, 1189–1205, https://doi.org/10.1175/JAS-D-20-0164.1.

——, ——, and S. W. Nesbitt, 2019: Using overshooting top area to discriminate potential for large, intense tornadoes. *Geophys. Res. Lett.*, **46**, 12 520–12 526, https://doi.org/10.1029/2019GL084099.

Markowski, P. M., 2020: What is the intrinsic predictability of tornadic supercell thunderstorms? *Mon. Wea. Rev.*, **148**, 3157–3180, https://doi.org/10.1175/MWR-D-20-0076.1.

——, and Y. Richardson, 2009: Tornadogenesis: Our current understanding, forecasting considerations, and questions to guide future research. *Atmos. Res.*, **93**, 3–10, https://doi.org/10.1016/j.atmosres.2008.09.015.

——, and ——, 2014: The influence of environmental low-level shear and cold pools on tornadogenesis: Insights from idealized simulations. *J. Atmos. Sci.*, **71**, 243–275, https://doi.org/10.1175/JAS-D-13-0159.1.

——, C. Hannon, J. Frame, E. Lancaster, A. Pietrycha, R. Edwards, and R. L. Thompson, 2003: Characteristics of vertical wind profiles near supercells obtained from the Rapid Update Cycle. *Wea. Forecasting*, **18**, 1262–1272, https://doi.org/10.1175/1520-0434(2003)018<1262:COVWPN>2.0.CO;2.

Marquis, J., Y. P. Richardson, P. Markowski, D. Dowell, and J. Wurman, 2012: Tornado maintenance investigated with high-resolution dual-Doppler and EnKF analysis. *Mon. Wea. Rev.*, **140**, 3–27, https://doi.org/10.1175/MWR-D-11-00025.1.

——, ——, ——, J. Wurman, K. Kosiba, and P. Robinson, 2016: An investigation of the Goshen County, Wyoming, tornadic supercell of 5 June 2009 using EnKF assimilation of mobile mesonet and radar observations collected during VORTEX2. Part II: Mesocyclone-scale processes affecting tornado formation, maintenance, and decay. *Mon. Wea. Rev.*, **144**, 3441–3463, https://doi.org/10.1175/MWR-D-15-0411.1.

McGraw, K. O., and S. P. Wong, 1992: A common language effect size statistic. *Psychol. Bull.*, **111**, 361–365, https://doi.org/10.1037/0033-2909.111.2.361.

McKeown, K. E., M. M. French, K. S. Tuftedal, D. M. Kingfield, H. B. Bluestein, D. W. Reif, and Z. B. Wienhoff, 2020: Rapid-scan and polarimetric radar observations of the dissipation of a violent tornado on 9 May 2016 near Sulphur, Oklahoma. *Mon. Wea. Rev.*, **148**, 3951–3971, https://doi.org/10.1175/MWR-D-20-0033.1.

Parker, M. D., 2014: Composite VORTEX2 supercell environments from near-storm soundings. *Mon. Wea. Rev.*, **142**, 508–529, https://doi.org/10.1175/MWR-D-13-00167.1.

Peters, J. M., C. J. Nowotarski, and H. Morrison, 2019: The role of vertical wind shear in modulating maximum supercell updraft velocities. *J. Atmos. Sci.*, **76**, 3169–3189, https://doi.org/10.1175/JAS-D-19-0096.1.

——, ——, J. P. Mulholland, and R. L. Thompson, 2020: The influences of effective inflow layer streamwise vorticity and storm-relative flow on supercell updraft properties. *J. Atmos. Sci.*, **77**, 3033–3057, https://doi.org/10.1175/JAS-D-19-0355.1.

Picca, J. C., M. R. Kumjian, and A. V. Ryzhkov, 2010: ZDR columns as a predictive tool for hail growth and storm evolution. *25th Conf. on Severe Local Storms*, Denver, CO, Amer. Meteor. Soc., 11.3, https://ams.confex.com/ams/25SLS/techprogram/paper_175750.htm.

——, J. C. Snyder, and A. V. Ryzhkov, 2015: An observational analysis of ZDR column trends in tornadic supercells. *37th Conf. on Radar Meteorology*, Norman, OK, Amer. Meteor. Soc., 5A.5, https://ams.confex.com/ams/37RADAR/webprogram/Paper275416.html.

Rasmussen, E. N., and D. O. Blanchard, 1998: A baseline climatology of sounding-derived supercell and tornado forecast parameters. *Wea. Forecasting*, **13**, 1148–1164, https://doi.org/10.1175/1520-0434(1998)013<1148:ABCOSD>2.0.CO;2.

Richardson, L. M., and R. Lee, 2019: An improved technique for estimating ZDR bias from light rain on radars that cannot vertically point. *39th Int. Conf. on Radar Meteorology*, Nara, Japan, Amer. Meteor. Soc., P3.21, https://www.roc.noaa.gov/wsr88d/PublicDocs/Publications/Richardson_Lee_2019_%20ImprovedTechniqueZDRBELRonRadarsThatCannotVerticallyPoint_39th_ICRM.pdf.

——, W. D. Zittel, R. R. Lee, V. M. Melnikov, R. L. Ice, and J. G. Cunningham, 2017: Bragg scatter detection by the WSR-88D. Part II: Assessment of Z_{DR} bias estimation. *J. Atmos. Oceanic Technol.*, **34**, 479–493, https://doi.org/10.1175/JTECH-D-16-0031.1.

Ripberger, J. T., C. L. Silva, H. C. Jenkins-Smith, and M. James, 2015: The influence of consequence-based messages on public responses to tornado warnings. *Bull. Amer. Meteor. Soc.*, **96**, 577–590, https://doi.org/10.1175/BAMS-D-13-00213.1.

Ryzhkov, A. V., V. B. Zhuravlyov, and N. A. Rybakova, 1994: Preliminary results of X-band polarization radar studies of clouds and precipitation. *J. Atmos. Oceanic Technol.*, **11**, 132–139, https://doi.org/10.1175/1520-0426(1994)011<0132:PROXBP>2.0.CO;2.

——, T. J. Schuur, D. W. Burgess, and D. S. Zrnic, 2005: Polarimetric tornado detection. *J. Appl. Meteor.*, **44**, 557–570, https://doi.org/10.1175/JAM2235.1.

Sandmæl, T. N., C. R. Homeyer, K. M. Bedka, J. M. Apke, J. R. Mecikalski, and K. Khlopenkov, 2019: Evaluating the ability of remote sensing observations to identify significantly severe and potentially tornadic storms. *J. Appl. Meteor.*, **58**, 2569–2590, https://doi.org/10.1175/JAMC-D-18-0241.1.

Segall, J. H., M. M. French, D. M. Kingfield, S. D. Loeffler, and M. R. Kumjian, 2021: Storm-scale polarimetric radar signatures associated with tornado dissipation in supercells. *Wea. Forecasting*, in press, https://doi.org/10.1175/WAF-D-21-0067.1.

Sessa, M. F., and R. J. Trapp, 2020: Observed relationship between tornado intensity and pretornadic mesocyclone characteristics. *Wea. Forecasting*, **35**, 1243–1261, https://doi.org/10.1175/WAF-D-19-0099.1.

Smith, B. T., R. L. Thompson, J. S. Grams, C. Broyles, and H. E. Brooks, 2012: Convective modes for significant severe thunderstorms in the contiguous United States. Part I: Storm classification and climatology. *Wea. Forecasting*, **27**, 1114–1135, https://doi.org/10.1175/WAF-D-11-00115.1.

——, ——, A. R. Dean, and P. T. Marsh, 2015: Diagnosing the conditional probability of tornado damage rating using environmental and radar attributes. *Wea. Forecasting*, **30**, 914–932, https://doi.org/10.1175/WAF-D-14-00122.1.

——, ——, D. A. Speheger, A. R. Dean, C. D. Karstens, and A. K. Anderson-Frey, 2020a: WSR-88D tornado intensity estimates. Part I: Real-time probabilities of peak tornado wind speeds. *Wea. Forecasting*, **35**, 2479–2492, https://doi.org/10.1175/WAF-D-20-0010.1.

——, ——, ——, ——, ——, and ——, 2020b: WSR-88D tornado intensity estimates. Part II: Real-time applications to tornado warning time scales. *Wea. Forecasting*, **35**, 2493–2506, https://doi.org/10.1175/WAF-D-20-0011.1.

Snyder, J. C., and H. B. Bluestein, 2014: Some considerations for the use of high-resolution mobile radar data in tornado intensity determination. *Wea. Forecasting*, **29**, 799–827, https://doi.org/10.1175/WAF-D-14-00026.1.

——, ——, V. Venkatesh, and S. J. Frasier, 2013: Observations of polarimetric signatures in supercells by an X-band mobile Doppler radar. *Mon. Wea. Rev.*, **141**, 3–29, https://doi.org/10.1175/MWR-D-12-00068.1.

——, A. V. Ryzhkov, M. R. Kumjian, A. P. Khain, and J. Picca, 2015: A Z_{DR} column detection algorithm to examine convective storm updrafts. *Wea. Forecasting*, **30**, 1819–1844, https://doi.org/10.1175/WAF-D-15-0068.1.

Thompson, R. L., R. Edwards, J. A. Hart, K. L. Elmore, and P. Markowski, 2003: Close proximity soundings within supercell environments obtained from the Rapid Update Cycle. *Wea. Forecasting*, **18**, 1243–1261, https://doi.org/10.1175/1520-0434(2003)018<1243:CPSWSE>2.0.CO;2.

——, B. T. Smith, J. S. Grams, A. R. Dean, and C. Broyles, 2012: Convective modes for significant severe thunderstorms in the contiguous United States. Part II: Supercell and QLCS tornado environments. *Wea. Forecasting*, **27**, 1136–1154, https://doi.org/10.1175/WAF-D-11-00116.1.

——, and Coauthors, 2017: Tornado damage rating probabilities derived from WSR-88D data. *Wea. Forecasting*, **32**, 1509–1528, https://doi.org/10.1175/WAF-D-17-0004.1.

Trapp, R. J., 1999: Observations of nontornadic low-level mesocyclones and attendant tornadogenesis failure during VORTEX. *Mon. Wea. Rev.*, **127**, 1693–1705, https://doi.org/10.1175/1520-0493(1999)127<1693:OONLLM>2.0.CO;2.

——, G. R. Marion, and S. W. Nesbitt, 2017: The regulation of tornado intensity by updraft width. *J. Atmos. Sci.*, **74**, 4199–4211, https://doi.org/10.1175/JAS-D-16-0331.1.

——, ——, and ——, 2018: Reply to ''Comments on 'The regulation of tornado intensity by updraft width.''' *J. Atmos. Sci.*, **75**, 4057–4061, https://doi.org/10.1175/JAS-D-18-0276.1.

Tuftedal, K. S., M. M. French, D. M. Kingfield, and J. C. Snyder, 2021: Observed bulk hook echo drop size distribution evolution in supercell tornadogenesis and tornadogenesis failure. *Mon. Wea. Rev.*, **149**, 2539–2557, https://doi.org/10.1175/MWR-D-20-0353.1.

Van Den Broeke, M. S., 2017: Polarimetric radar metrics related to tornado life cycles and intensity in supercell storms. *Mon. Wea. Rev.*, **145**, 3671–3686, https://doi.org/10.1175/MWR-D-16-0453.1.

——, 2020: A preliminary polarimetric radar comparison of pretornadic and nontornadic supercell storms. *Mon. Wea. Rev.*, **148**, 1567–1584, https://doi.org/10.1175/MWR-D-19-0296.1.

Vargha, A., and H. Delaney, 2000: A critique and improvement of the ''CL'' common language effect size statistics of McGraw and Wong. *J. Educ. Behav. Stat.*, **25**, 101–132.

Warren, R. A., H. Richter, H. A. Ramsay, S. T. Siems, and M. J. Manton, 2017: Impact of variations in upper-level shear on simulated supercells. *Mon. Wea. Rev.*, **145**, 2659–2681, https://doi.org/10.1175/MWR-D-16-0412.1.

Witt, A., M. D. Eilts, G. J. Stumpf, E. D. W. Mitchell, J. T. Johnson, and K. W. Thomas, 1998: Evaluating the performance of WSR-88D severe storm detection algorithms. *Wea. Forecasting*, **13**, 513–518, https://doi.org/10.1175/1520-0434(1998)013<0513:ETPOWS>2.0.CO;2.

Wood, V. T., and R. A. Brown, 1997: Effects of radar sampling on single-Doppler velocity signatures of mesocyclones and tornadoes. *Wea. Forecasting*, **12**, 928–938, https://doi.org/10.1175/1520-0434(1997)012<0928:EORSOS>2.0.CO;2.

Wurman, J., D. Dowell, Y. Richardson, P. Markowski, E. Rasmussen, D. Burgess, L. Wicker, and H. B. Bluestein, 2012: The Second Verification of the Origins of Rotation in Tornadoes Experiment: VORTEX2. *Bull. Amer. Meteor. Soc.*, **93**, 1147–1170, https://doi.org/10.1175/BAMS-D-11-00010.1.

——, K. Kosiba, T. White, and P. Robinson, 2021: Supercell tornadoes are much stronger and wider than damage-based ratings indicate. *Proc. Natl. Acad. Sci.*, **118**, e2021535118, https://doi.org/10.1073/pnas.2021535118.